Shunts vs. networks: tuning and comparison of centralized and decentralized piezoelectric vibration absorbers

G Raze[1], J Dietrich[1], B Lossouarn[2] and G Kerschen[1]

[1] Space Structures and Systems Laboratory, Aerospace and Mechanical Engineering Department, University of Liège, Quartier Polytech 1 (B52/3), Allée de la Découverte 9, B-4000 Liège, Belgium

[2] Laboratoire de Mécanique des Structures et des Systèmes Couplés, Conservatoire national des arts et métiers, Rue Saint-Martin 292, 75003 Paris, France

E-mail: g.raze@uliege.be

Abstract. This work develops a unified modeling framework for piezoelectric structures controlled by passive shunts connected to a single transducer and/or networks interconnecting multiple transducers. A common tuning procedure for these different control approaches, termed decentralized and centralized approaches, respectively, is proposed. The generic model is then used to compare them in terms of vibration mitigation performance. It is shown that decentralization can be detrimental to performance in general. Digital vibration absorbers are then leveraged to realize the shunts and/or networks. In this regard, the proposed tuning procedure solely relies on characteristics that can be identified from the digital units of these absorbers. The theoretical developments are numerically and experimentally validated on piezoelectric beams.

Keywords: Piezoelectric shunt, Electrical network, Multimodal vibration mitigation, Passive control, Digital vibration absorber

Submitted to: *Smart Mater. Struct.*

1. Introduction

Since the pioneering works of Forward [1] and Hagood and von Flotow [2], piezoelectric damping has gained wide interest and has become an active research field [3]. With this vibration mitigation technique, the ability of piezoelectric transducers to convert mechanical energy into electrical energy is leveraged to dissipate the latter into circuits connecting their electrodes, and/or to reuse it to provide a counter action. These circuits, commonly called shunts, are generally resistive or resonant. Resonant shunts combine resistive and inductive (RL) elements to enhance energy dissipation via a resonance of the shunt with the inherent capacitance of the transducer, thereby resulting in effective vibration mitigation. In practice, resonant shunts are realized using analog [4, 5] or digital [6] electronics. The use of fully passive inductors with high inductances was also demonstrated to be possible [7]. Recently, accurate characterization [8] and calibration [9, 10] techniques were proposed to optimize the performance of piezoelectric shunts. A number of works also aimed to extend this approach to the control of multiple structural modes.

When the structure is equipped with a single transducer, a multi-resonant circuit can be connected to it in order to achieve multimodal damping. An overview of the different circuits that can be used for this purpose can be found in [11]. A unified tuning approach for these shunts was proposed in [12], and it was also shown therein that they are all approximately equal in terms of vibration mitigation performance. Alternatively, other approaches were proposed to optimize the characteristics of circuits without prescribing their topologies [13, 14].

Piezoelectric structures may also be endowed with multiple transducers to ensure substantial coupling with several vibration modes. A straightforward approach to achieve multimodal damping then consists in shunting each of these transducers individually with classical RL [15, 16] or multi-resonant [17, 18] shunts. Alternatively, a multi-terminal electrical network that interconnects the transducers can be designed. In the control theory terminology, the former and latter approaches are named decentralized and centralized control, respectively [19, 20]. Networks are traditionally tuned to be electrical analogs of the structure they are connected to, i.e., they feature the same resonance frequencies and mode shapes as their host [21]. This approach has been experimentally validated on academic structures [22, 23] and could be extended to more complex structures by assembling various analog networks [24] and to nonlinear structures by using a principle of similarity [25]. Similarly to multi-resonant shunts, alternate methods were proposed to tune networks of unprescribed topologies [26, 27, 28].

Comparisons between shunts and networks are rather scarce in the literature. Giorgio [17] and Rosi [18] highlighted the superior performance of networks over that of shunts. Trindade *et al* [29] compared the performance and robustness of RL shunts with those of a network targeting a single mode. They concluded that the latter tends to be more robust than the former. However, there does not exist a unified model allowing to

predict how such approaches can be compared in terms of performance.

In this light, this work aims to provide tools to compare passive centralized and decentralized piezoelectric damping techniques where one electrical resonant mode targets one mechanical mode. First, a common modeling framework encompassing all the aforementioned approaches for multimodal damping is developed. Second, a unified tuning procedure is proposed. Third, the theoretical developments are exploited to draw conclusions on the performance of the different strategies. A further objective of this work is to leverage digital vibration absorbers (DVAs) to develop a model-less tuning approach allowing for the realization of shunts or networks. Consequently, the tuning procedure only requires characteristics of the host system that are identifiable from the DVAs.

This work is organized as follows. Section 2 presents a model of a piezoelectric structure coupled to a set DVAs emulating a passive network, and introduces the effect of decentralization. The absorbers' tuning is addressed in Section 3. The resulting performance is discussed in Section 4 and numerically illustrated with a free-free piezoelectric beam. Finally, the theoretical developments are numerically verified and experimentally validated with a clamped-free piezoelectric beam in Section 5.

2. Dynamics of a piezoelectric structure connected to a set of DVAs

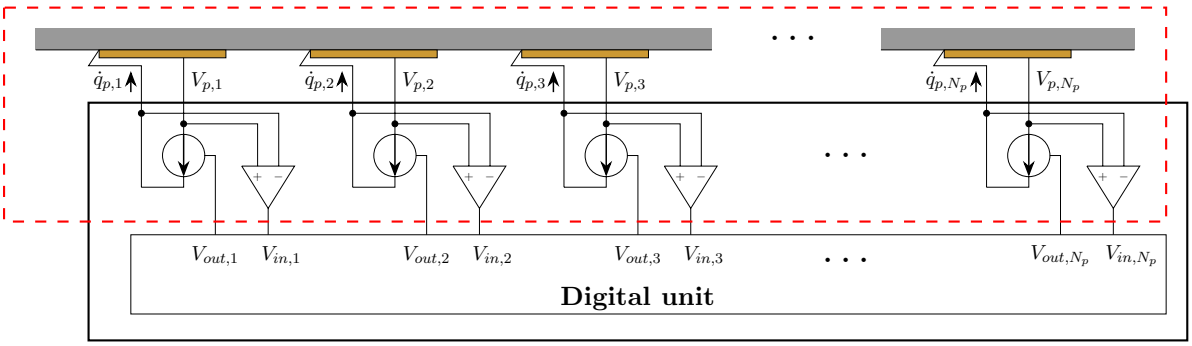

Figure 1: Schematic representation of a structure (in gray) with N_p piezoelectric transducers (in orange) connected to a multiport DVA (in white); the red dashed frame represents the host system as seen by the digital unit.

The DVA was first proposed by Fleming *et al* [6] as a versatile means to realize virtually any circuit or network. By measuring the voltages of the transducers, the currents to be injected back into them are computed by a digital unit in order to mimic the action of an electrical assembly. Figure 1 schematically represents a multiport DVA interconnecting multiple transducers.

In this section, the dynamic equations of a structure controlled by a set of multi-resonant, centralized or decentralized DVAs are derived. It is assumed that the characteristics of the networks or shunts emulated by the DVAs are known, which allows for the quantification of the electromechanical coupling between the structural

and electrical modes. These derivations will then be exploited in the next section to tune the characteristics of the DVAs.

2.1. Governing equations of the host structure

Considering an undamped N-degree-of-freedom structure endowed with N_p piezoelectric transducers, the vectors of N generalized degrees of freedom $\mathbf{x}$ and generalized loadings $\mathbf{f}$ and the vectors of N_p piezoelectric voltages $\mathbf{V}_p$ and charges $\mathbf{q}_p$ are dynamically related by the governing equations

$$\begin{cases} \left(s^2\mathbf{M} + \mathbf{K}_{oc}\right)\mathbf{x} - \boldsymbol{\Theta}\mathbf{q}_p = \mathbf{f} \\ \boldsymbol{\Theta}^T\mathbf{x} - \mathbf{E}_p^{\varepsilon}\mathbf{q}_p = \mathbf{V}_p \end{cases}, \tag{1}$$

where $\mathbf{M}$, and $\mathbf{K}_{oc}$ are $N \times N$ structural mass and open-circuit stiffness matrices, respectively, $\boldsymbol{\Theta}$ is a $N \times N_p$ piezoelectric coupling matrix, $\mathbf{E}_p^{\varepsilon}$ is the $N_p \times N_p$ piezoelectric elastance (inverse of capacitance) matrix at constant strain of the transducers, and s is Laplace's variable [30, 31]. The mass-normalized open-circuit modes are defined by

$$\mathbf{K}_{oc}\boldsymbol{\Phi}_{oc} = \mathbf{M}\boldsymbol{\Phi}_{oc}\boldsymbol{\Omega}_{oc}^2, \qquad \boldsymbol{\Phi}_{oc}^T\mathbf{M}\boldsymbol{\Phi}_{oc} = \mathbf{I}, \qquad \mathbf{x} = \boldsymbol{\Phi}_{oc}\boldsymbol{\eta}_{oc}, \tag{2}$$

where $\boldsymbol{\Phi}_{oc}$ is the $N \times N$ open-circuit mode shape matrix, $\boldsymbol{\Omega}_{oc} = \mathbf{diag}\left(\omega_{oc,1}, \cdots, \omega_{oc,N}\right)$ is a diagonal matrix containing the circular open-circuit resonance frequencies, $\boldsymbol{\eta}_{oc}$ is a vector of N modal coordinates and $\mathbf{I}$ is the identity matrix. With Equation (2), Equation (1) can also be rewritten in modal form as

$$\begin{cases} \left(s^2\mathbf{I} + \boldsymbol{\Omega}_{oc}^2\right)\boldsymbol{\eta}_{oc} - \boldsymbol{\Theta}_{\Phi}\mathbf{q}_p = \boldsymbol{\Phi}_{oc}^T\mathbf{f} \\ \boldsymbol{\Theta}_{\Phi}^T\boldsymbol{\eta}_{oc} - \mathbf{E}_p^{\varepsilon}\mathbf{q}_p = \mathbf{V}_p \end{cases}, \tag{3}$$

where $\boldsymbol{\Theta}_{\Phi} = \boldsymbol{\Phi}_{oc}^T\boldsymbol{\Theta}$ is a $N \times N_p$ modal piezoelectric coupling matrix.

2.2. Governing equations of the controlled system

A multiport DVA is now connected to the transducers of the host structure as shown in Figure 1, and the dynamics of this system are analyzed. Assuming that the digital unit input $\mathbf{V}_{in}$ and output $\mathbf{V}_{out}$ are proportional to the piezoelectric voltages and currents, respectively, these signals are given by

$$\mathbf{V}_{in} = \mathbf{G}_{in}\mathbf{V}_p \qquad \text{and} \qquad s\mathbf{q}_p = \mathbf{G}_{out}\mathbf{V}_{out}. \tag{4}$$

In principle, $\mathbf{G}_{in}$ and $\mathbf{G}_{out}$ should be invertible diagonal matrices representing the voltage sensors and current sources gains, respectively. In the mathematical framework considered herein, they only need to be full rank. With Equation (4), the governing equations of the host system (Equation (3)) become

$$\begin{cases} \left(s^2\mathbf{I} + \boldsymbol{\Omega}_{oc}^2\right)\boldsymbol{\eta}_{oc} - s^{-1}\mathbf{B}\mathbf{V}_{out} = \boldsymbol{\Phi}_{oc}^T\mathbf{f} \\ \mathbf{C}\boldsymbol{\eta}_{oc} - s^{-1}\mathbf{D}\mathbf{V}_{out} = \mathbf{V}_{in} \end{cases}, \tag{5}$$

where

$$\mathbf{B} = \boldsymbol{\Theta}_{\Phi}\mathbf{G}_{out}, \qquad \mathbf{C} = \mathbf{G}_{in}\boldsymbol{\Theta}_{\Phi}^T, \qquad \mathbf{D} = \mathbf{G}_{in}\mathbf{E}_p^{\varepsilon}\mathbf{G}_{out}. \tag{6}$$

These matrices may be identified experimentally using only the DVAs. Indeed, by injecting a current in the system through the signal $\mathbf{V}_{out}$ and measuring its response through $\mathbf{V}_{in}$, state-of-the-art identification techniques can be used to deduce $\mathbf{B}$, $\mathbf{C}$, $\mathbf{D}$ and $\boldsymbol{\Omega}_{oc}$. Examples of such techniques include subspace identification [32], eigensystem realization [33] or polyreference least-squares complex frequency-domain methods [34]. This advocates the development of a tuning approach solely exploiting the matrices given in Equation (5), which models the system inside the red dashed frame in Figure 1. In this way, one can tune the DVAs for effective multimodal vibration mitigation without the need to build a sophisticated numerical model of the host structure and/or to use any external excitation device.

The set of DVAs connected to the transducers can be programmed such that they impose an input-output relation governed by the impedance matrix $\mathbf{Z}_{DVA}$

$$\mathbf{V}_{in} = \mathbf{Z}_{DVA}(s)\mathbf{V}_{out} \tag{7}$$

so that, using the electrical part of Equation (5),

$$\mathbf{C}\boldsymbol{\eta}_{oc} = \left(\mathbf{D} + s\mathbf{Z}_{DVA}(s)\right) s^{-1}\mathbf{V}_{out}. \tag{8}$$

$\mathbf{Z}_{DVA}$ can be designed in order to create a network that resonates with the piezoelectric transducers at N_e frequencies, i.e.,

$$\boldsymbol{\Phi}_{in}^T \left(\mathbf{D} + s\mathbf{Z}_{DVA}(s)\right) \boldsymbol{\Phi}_{out} = s^2\boldsymbol{\Omega}_e^{-2} + 2s\mathbf{Z}_e\boldsymbol{\Omega}_e^{-1} + \mathbf{I}, \tag{9}$$

where $\boldsymbol{\Phi}_{in}$ and $\boldsymbol{\Phi}_{out}$ are the network input and output mode shapes, respectively, of size $N_p \times N_e$, and $\boldsymbol{\Omega}_e = \mathbf{diag}\left(\omega_{e,1}, \cdots, \omega_{e,N_e}\right)$ and $\mathbf{Z}_e = \mathbf{diag}\left(\zeta_{e,1}, \cdots, \zeta_{e,N_e}\right)$ are diagonal matrices containing the electrical resonance frequencies and damping ratios, respectively. The electrical input and output mode shapes are distorted versions of the electrical mode shapes of a passive network $\boldsymbol{\Phi}_p$. This distortion is introduced to compensate for the input and output gain matrices. When these gain matrices are equal to the identity, the mode shape matrices are all identical (see Equation (A.7)). If electrical modal coordinates $\boldsymbol{\eta}_e$ are introduced such that

$$s^{-1}\mathbf{V}_{out} = \boldsymbol{\Phi}_{out}\boldsymbol{\eta}_e, \tag{10}$$

the combination of Equations (7)-(10) inserted into Equation (5) gives the governing equations of the electromechanical system

$$\begin{cases} \left(s^2\mathbf{I} + \boldsymbol{\Omega}_{oc}^2\right)\boldsymbol{\eta}_{oc} - \mathbf{B}\boldsymbol{\Phi}_{out}\boldsymbol{\eta}_e = \boldsymbol{\Phi}_{oc}^T\mathbf{f} \\ \left(s^2\boldsymbol{\Omega}_e^{-2} + 2s\mathbf{Z}_e\boldsymbol{\Omega}_e^{-1} + \mathbf{I}\right)\boldsymbol{\eta}_e - \boldsymbol{\Phi}_{in}^T\mathbf{C}\boldsymbol{\eta}_{oc} = 0 \end{cases}. \tag{11}$$

These equations express the dynamics in terms of resonant mechanical and electrical modal coordinates, and can be seen as a generalization of the governing equations for a single-degree-of-freedom structure controlled with a RL shunt (see, e.g., [2, 35]). By matching the electrical resonance frequencies to those of the structure and properly tailoring the electrical mode shapes and damping ratios, effective multimodal damping can be achieved [21, 24, 28].

The DVAs are programmed to mimic the action of a passive network in this work. This results in a control apparatus featuring satisfactory performance with advantageous

stability properties [26]. The extension to purely active control appears to be possible but is beyond the scope of the present article. The conditions under which the DVAs emulate a passive network are derived in Appendix A.1. The input and output mode shapes are chosen to satisfy the condition

$$\mathbf{B}\boldsymbol{\Phi}_{out} = \mathbf{C}^T\boldsymbol{\Phi}_{in}. \tag{12}$$

Due to possible errors that may arise during the experimental identification, this equality may not exactly hold. However, the input and output electrical mode shapes can be chosen so as to make this error minimum in the least-squares sense. The departure from equality will thus be small and shall be neglected in the sequel.

A passivity constraint limiting the amplitude of the electrical mode shapes is also derived as

$$\mathbf{I} - \boldsymbol{\Phi}_{in}^T\mathbf{D}\boldsymbol{\Phi}_{out} \succeq 0, \tag{13}$$

where $\succeq 0$ denotes that the matrix has non-negative eigenvalues.

It should finally be noted that the case $\mathbf{G}_{in} = \mathbf{G}_{out} = \mathbf{I}$ corresponds to an actual passive network, similarly to, e.g., [17, 28]. The model developed herein is thus more general and allows for the development of the model-less tuning procedure proposed herein.

2.3. Decentralized set of DVAs

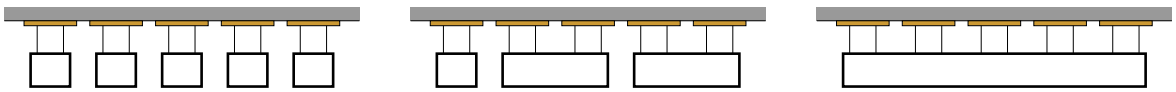

Figure 2: Schematic representation of a structure (in gray) with piezoelectric transducers (in orange) connected to decentralized (a), partially decentralized (b) and centralized (c) absorbers (in white).

It is now assumed that the transducers and DVAs are grouped into N_g independent groups. Figure 2 schematizes several examples of such groups. We note that this formalism can represent a fully decentralized situation (i.e., individually-shunted transducers) when $N_g = N_p$, or a fully centralized network when $N_g = 1$. The collective dynamics of the groups can be expressed under the form of an equivalent, global network. Indeed, the matrices of electrical resonance frequencies and damping ratios can be built as block diagonal ones as

$$\boldsymbol{\Omega}_e = \mathbf{blkdiag}\left(\boldsymbol{\Omega}_e^{(1)}\ ,\ \boldsymbol{\Omega}_e^{(2)}\ ,\ \cdots\ ,\ \boldsymbol{\Omega}_e^{(N_g)}\right), \tag{14}$$

$$\mathbf{Z}_e = \mathbf{blkdiag}\left(\mathbf{Z}_e^{(1)}\ ,\ \mathbf{Z}_e^{(2)}\ ,\ \cdots\ ,\ \mathbf{Z}_e^{(N_g)}\right), \tag{15}$$

where $\boldsymbol{\Omega}_e^{(g)}$ and $\mathbf{Z}_e^{(g)}$ are the matrices of electrical resonance frequencies and damping ratios, respectively, of group g. Assuming group g targets $N_e^{(g)}$ modes, these matrices

dimensions are $N_e^{(g)} \times N_e^{(g)}$. Similarly, the input and output mode shapes are sought to be determined independently on each group as

$$\mathbf{\Phi}_{in} = \mathbf{blkdiag}\left(\mathbf{\Phi}_{in}^{(1)}\ ,\ \mathbf{\Phi}_{in}^{(2)}\ ,\ \cdots\ ,\ \mathbf{\Phi}_{in}^{(N_g)}\right), \tag{16}$$

$$\mathbf{\Phi}_{out} = \mathbf{blkdiag}\left(\mathbf{\Phi}_{out}^{(1)}\ ,\ \mathbf{\Phi}_{out}^{(2)}\ ,\ \cdots\ ,\ \mathbf{\Phi}_{out}^{(N_g)}\right). \tag{17}$$

A decentralized implementation is only possible if $\mathbf{D}$ itself has a block diagonal structure (this claim will be justified hereafter in Section (3.3)). The non-block-diagonal terms are generally small and can be neglected (this assumption is further discussed in the supplementary materials of this article). Hence, $\mathbf{D}$ is decomposed into

$$\mathbf{D} = \mathbf{D}_{BD} + \mathbf{D}_{ND}, \tag{18}$$

where $\mathbf{D}_{BD}$ is a block diagonal matrix whose diagonal blocks are equal to those of $\mathbf{D}$, i.e.,

$$\mathbf{D}_{BD} = \mathbf{blkdiag}\left(\mathbf{D}^{(1)}\ ,\ \cdots\ ,\ \mathbf{D}^{(N_g)}\right), \tag{19}$$

with $\mathbf{D}^{(g)}$ the restriction of $\mathbf{D}$ to the electrical degrees of freedom of group g. $\mathbf{D}_{ND}$ then contains the non-diagonal blocks (for a fully centralized network, $\mathbf{D} = \mathbf{D}^{(1)} = \mathbf{D}_{BD}$ and $\mathbf{D}_{ND} = \mathbf{0}$). The electrical mode shapes will be tuned ignoring the latter, i.e., setting them considering that Equation (9) is replaced by

$$\mathbf{\Phi}_{in}^T \left(\mathbf{D}_{BD} + s\mathbf{Z}_{DVA}(s)\right) \mathbf{\Phi}_{out} = s^2\mathbf{\Omega}_e^{-2} + 2s\mathbf{Z}_e\mathbf{\Omega}_e^{-1} + \mathbf{I}. \tag{20}$$

2.4. Modal electromechanical coupling

The electromechanical coupling between resonant mechanical and electrical modes is now assessed. It is a key factor for the absorbers' performance, because the greater this coupling, the greater the attenuation [36]. In a similar spirit to [28], the coupling is evaluated by considering that a mechanical mode is targeted by (at most) one electrical mode per group, and that these modes resonate together. Hence, in Equation (11), a single mechanical resonant mode r and corresponding electrical resonant modes (distributed over the groups targeting that mode) indexed by $\mathbf{k}$ are considered, while every other mode is assumed to be quiescent. This leads to the reduced dynamical equations

$$\begin{cases} \left(s^2 + \omega_{oc,r}^2\right)\eta_{oc,r} - \mathbf{b}_r\mathbf{\Phi}_{out,\mathbf{k}}\boldsymbol{\eta}_{e,\mathbf{k}} = \boldsymbol{\phi}_{oc,r}^T\mathbf{f} \\ \left(s^2\mathbf{\Omega}_{e,\mathbf{k}}^{-2} + 2s\mathbf{Z}_{e,\mathbf{k}}\mathbf{\Omega}_{e,\mathbf{k}}^{-1} + \mathbf{I}\right)\boldsymbol{\eta}_{e,\mathbf{k}} - \mathbf{\Phi}_{in,\mathbf{k}}^T\mathbf{c}_r\eta_{oc,r} = 0 \end{cases}, \tag{21}$$

where $\mathbf{b}_r$ and $\mathbf{c}_r$ are the r^{th} line of $\mathbf{B}$ and column of $\mathbf{C}$, respectively. Condensing the electrical equations into the mechanical one yields

$$\left\{\left(s^2 + \omega_{oc,r}^2\right) - \mathbf{b}_r\mathbf{\Phi}_{out,\mathbf{k}}\left(s^2\mathbf{\Omega}_{e,\mathbf{k}}^{-2} + 2s\mathbf{Z}_{e,\mathbf{k}}\mathbf{\Omega}_{e,\mathbf{k}}^{-1} + \mathbf{I}\right)^{-1}\mathbf{\Phi}_{in,\mathbf{k}}^T\mathbf{c}_r\right\}\eta_{oc,r} = \boldsymbol{\phi}_{oc,r}^T\mathbf{f}. \tag{22}$$

Similarly to shunts, modal-short- and modal-open-circuit resonance frequencies, $\widehat{\omega}_{sc,r}$ and $\widehat{\omega}_{oc,r}$, can be found by evaluating the limit of the term coming from the

electromechanical interaction for $s \to 0$ and $s \to \infty$, respectively [37]. When $s \to \infty$, this term tends to zero and thus $\widehat{\omega}_{oc,r} = \omega_{oc,r}$. As for the case when $s \to 0$,

$$\widehat{\omega}_{sc,r}^2 = \omega_{oc,r}^2 - \mathbf{b}_r \mathbf{\Phi}_{out,\mathbf{k}} \mathbf{\Phi}_{in,\mathbf{k}}^T \mathbf{c}_r. \tag{23}$$

A modal electromechanical coupling factor (MEMCF) $\alpha_{c,r\mathbf{k}}$ can be defined by‡

$$\alpha_{c,r\mathbf{k}}^2 = \frac{\widehat{\omega}_{oc,r}^2 - \widehat{\omega}_{sc,r}^2}{\widehat{\omega}_{oc,r}^2} = \frac{1}{\omega_{oc,r}^2} \mathbf{b}_r \mathbf{\Phi}_{out,\mathbf{k}} \mathbf{\Phi}_{in,\mathbf{k}}^T \mathbf{c}_r \tag{24}$$

and, using Equation (12), the MEMCF can also be expressed as

$$\alpha_{c,r\mathbf{k}} = \frac{1}{\omega_{oc,r}} ||\mathbf{b}_r \mathbf{\Phi}_{out,\mathbf{k}}|| = \frac{1}{\omega_{oc,r}} ||\mathbf{\Phi}_{in,\mathbf{k}}^T \mathbf{c}_r||, \tag{25}$$

where $||\cdot||$ represents the Euclidean norm of a vector. Decomposing the modal coupling vector into contributions from each group, the MEMCF becomes

$$\alpha_{c,r\mathbf{k}} = \frac{1}{\omega_{oc,r}} \sqrt{\sum_{g=1}^{N_g} \left(\mathbf{b}_r^{(g)} \boldsymbol{\phi}_{out,k}^{(g)} \right)^2}, \tag{26}$$

with $\mathbf{b}_r = \left[\mathbf{b}_r^{(1)} \ , \ \cdots \ , \ \mathbf{b}_r^{(N_g)} \right]$ and $\mathbf{\Phi}_{out,\mathbf{k}} = \mathbf{blkdiag}\left(\boldsymbol{\phi}_{out,k}^{(1)} \ , \ \cdots \ , \ \boldsymbol{\phi}_{out,k}^{(N_g)} \right)$. It should be emphasized that this MEMCF is related to the *network*, and it might differ from that of the *transducers* (measured by the normalized difference in resonance frequencies when the transducers are all in short and open circuit), which is a given characteristic of the host system.

3. Tuning of centralized and decentralized absorbers

The dynamics and coupling characteristics derived in the previous section are now exploited to tune the DVAs. Specifically, the electrical mode shapes, resonance frequencies and damping ratios are optimized to provide effective multimodal vibration mitigation of the controlled structure. The host system is assumed to be given, with fixed characteristics (including the size, position and materials of the transducers). The electrical mode shapes are first tailored to maximize the modal electromechanical coupling of the network with the targeted resonances of the host system. The electrical resonance frequencies and damping ratios are then tuned in adequacy with this coupling. Finally, the realization of the resulting shunt(s) and/or network(s) using DVAs is discussed.

3.1. Optimal input and output mode shapes

It is now sought to find input and output mode shapes maximizing the electromechanical coupling with the mode they target while respecting the passivity constraint. According

‡ In the field of piezoelectric shunts, the short-circuit resonance frequency is more commonly used for normalization [2]. The other convention is used in this section for simplicity, but there is little difference between the two normalizations in practice.

to Equation (26), the MEMCF is maximized if the terms inside the sum, representing the action of each group, are themselves maximized. Hence, an objective function can be defined as the weighted sum of these terms for every targeted mode as

$$\sum_{r=1}^{N_e}\sum_{g=1}^{N_g} w_r^{(g)} \frac{1}{\omega_{oc,r}} \mathbf{b}_r^{(g)} \boldsymbol{\phi}_{out,k}^{(g)} = \sum_{g=1}^{N_g} \mathrm{Tr}\left(\mathbf{W}^{(g)} \boldsymbol{\Omega}_{oc}^{-1} \mathbf{B}^{(g)} \boldsymbol{\Phi}_{out}^{(g)}\right), \tag{27}$$

where Tr denotes the trace operator, and the (positive) coefficients $w_r^{(g)}$ are chosen by the designer to weight the desired control authority over the modes targeted by group g. These weights are gathered in a diagonal matrix $\mathbf{W}^{(g)} = \mathbf{diag}\left(w_1^{(g)}, \cdots, w_{N_e^{(g)}}^{(g)}\right)$ and $\mathbf{B}^{(g)}$ is the restriction of $\mathbf{B}$ to the electrical degrees of freedom of group g. Including the passivity constraint (Equation (13)), the optimal electrical mode shapes are thus chosen to be the solution of the constrained optimization problem

$$\begin{array}{ll} \underset{\boldsymbol{\Phi}_{in},\boldsymbol{\Phi}_{out}}{\text{Maximize}} & \sum_{g=1}^{N_g} \mathrm{Tr}\left(\mathbf{W}^{(g)} \boldsymbol{\Omega}_{oc}^{-1} \mathbf{B}^{(g)} \boldsymbol{\Phi}_{out}^{(g)}\right) \\ \text{Subject to} & \mathbf{I} - \boldsymbol{\Phi}_{in}^T \mathbf{D} \boldsymbol{\Phi}_{out} \succeq 0 \end{array}. \tag{28}$$

If the matrix $\mathbf{D}$ is block diagonal, or if its non-block diagonal part is neglected (i.e., $\mathbf{D} \approx \mathbf{D}_{BD}$), the passivity constraint is decoupled on each group (Equations (17) and (19)). Finally, we note that the objective function consists of independent contributions from each group as well. The optimization problem can therefore be solved group by group as

$$\begin{array}{ll} \underset{\boldsymbol{\Phi}_{in}^{(g)},\boldsymbol{\Phi}_{out}^{(g)}}{\text{Maximize}} & \mathrm{Tr}\left(\mathbf{W}^{(g)} \boldsymbol{\Omega}_{oc}^{-1} \mathbf{B}^{(g)} \boldsymbol{\Phi}_{out}^{(g)}\right) \\ \text{Subject to} & \mathbf{I} - \left(\boldsymbol{\Phi}_{in}^{(g)}\right)^T \mathbf{D}^{(g)} \boldsymbol{\Phi}_{out}^{(g)} \succeq 0 \end{array}, \qquad g \in [1\ ,\ \cdots\ ,\ N_g]\,. \tag{29}$$

An analytical solution to this optimization problem can be found (see Appendix A.2 for the proof). Let the singular value decomposition (SVD) of $\mathbf{D}^{(g)}$ be given by

$$\mathbf{D}^{(g)} = \mathbf{U}_D^{(g)} \boldsymbol{\Sigma}_D^{(g)} \left(\mathbf{V}_D^{(g)}\right)^T. \tag{30}$$

Modified input and output matrices are built as

$$\mathbf{B}^{(g)} \mathbf{V}_D^{(g)} \left(\boldsymbol{\Sigma}_D^{(g)}\right)^{-1/2} = \left[\begin{array}{ccc} \left(\mathbf{b}_{D,1}^{(g)}\right)^T & \cdots & \left(\mathbf{b}_{D,N_e^{(g)}}^{(g)}\right)^T \end{array}\right]^T, \tag{31}$$

$$\left(\mathbf{C}^{(g)}\right)^T \mathbf{U}_D^{(g)} \left(\boldsymbol{\Sigma}_D^{(g)}\right)^{-1/2} = \left[\begin{array}{ccc} \left(\mathbf{c}_{D,1}^{(g)}\right)^T & \cdots & \left(\mathbf{c}_{D,N_e^{(g)}}^{(g)}\right)^T \end{array}\right]^T, \tag{32}$$

and a scaling matrix $\mathbf{S}^{(g)} = \mathbf{diag}\left(s_1^{(g)}, \cdots, s_{N_e^{(g)}}^{(g)}\right)$ whose elements are built from the rows of these modified input and output matrices as

$$s_k^{(g)} = \sqrt{\frac{||\mathbf{c}_{D,k}^{(g)}||}{||\mathbf{b}_{D,k}^{(g)}||}}, \qquad k \in [1, \cdots, N_e^{(g)}]. \tag{33}$$

Finally, given the compact SVD

$$\mathbf{S}^{(g)} \mathbf{W}^{(g)} \boldsymbol{\Omega}_{oc}^{-1} \mathbf{B}^{(g)} \mathbf{V}_D^{(g)} \left(\boldsymbol{\Sigma}_D^{(g)}\right)^{-1/2} = \mathbf{U}_M^{(g)} \boldsymbol{\Sigma}_M^{(g)} \left(\mathbf{V}_M^{(g)}\right)^T, \tag{34}$$

optimal input and output mode shapes are given by

$$\mathbf{\Phi}_{in}^{(g)} = \mathbf{U}_D^{(g)} \left(\mathbf{\Sigma}_D^{(g)}\right)^{-1/2} \mathbf{\Psi}^{(g)} \left(\mathbf{S}^{(g)}\right)^{-1} \tag{35}$$

and

$$\mathbf{\Phi}_{out}^{(g)} = \mathbf{V}_D^{(g)} \left(\mathbf{\Sigma}_D^{(g)}\right)^{-1/2} \mathbf{\Psi}^{(g)} \mathbf{S}^{(g)}, \tag{36}$$

respectively, with the optimal dimensionless electrical mode shape matrix

$$\mathbf{\Psi}^{(g)} = \mathbf{V}_M^{(g)} \left(\mathbf{U}_M^{(g)}\right)^T, \tag{37}$$

with which the passivity constraint becoming

$$\mathbf{I} - \left(\mathbf{\Psi}^{(g)}\right)^T \mathbf{\Psi}^{(g)} \succeq 0 \tag{38}$$

is respected. Further elaboration on these results is made in Section 4, but the complete tuning procedure is first presented in the foregoing section.

3.2. Optimal electrical resonance frequencies and damping ratios

It is now possible to tune the resonance frequencies and damping ratios of the networks. To comply with the normalization used in [38], an MEMCF normalized with the short-circuit frequency is computed from Equation (24) as

$$K_{c,r\mathbf{k}}^2 = \frac{\widehat{\omega}_{oc,r}^2 - \widehat{\omega}_{sc,r}^2}{\widehat{\omega}_{sc,r}^2} = \frac{\alpha_{c,r\mathbf{k}}^2}{1 - \alpha_{c,r\mathbf{k}}^2}. \tag{39}$$

Using the resonance frequency $\omega_{oc,r}$ and the MEMCF in the optimal tuning rule derived by Soltani *et al* [35, 38], an intermediate parameter given by

$$r_{e,k} = \frac{\sqrt{64 - 16K_{c,r\mathbf{k}}^2 - 26K_{c,r\mathbf{k}}^4} - K_{c,r\mathbf{k}}^2}{8}, \tag{40}$$

is used to compute the optimal electrical resonant frequency and damping ratio as

$$\omega_{e,k} = \sqrt{\frac{3K_{c,r\mathbf{k}}^2 - 4r_{e,k} + 8}{4K_{c,r\mathbf{k}}^2 + 4}}\omega_{oc,r} \tag{41}$$

and

$$\zeta_{e,k} = \frac{\sqrt{27K_{c,r\mathbf{k}}^4 + 80K_{c,r\mathbf{k}}^2 + 64 - 16r_{e,k}\left(4 + 3K_{c,r\mathbf{k}}^2\right)}}{\sqrt{2}\left(5K_{c,r\mathbf{k}}^2 + 8\right)}, \tag{42}$$

respectively. Eventually, the optimal electrical resonance frequency and damping ratio are attributed to each group by simply setting

$$\mathbf{\Omega}_{e,k}^{-2} = \omega_{e,k}^{-2}\mathbf{I} \tag{43}$$

and

$$\mathbf{Z}_{e,k} = \zeta_{e,k}\mathbf{I}, \tag{44}$$

respectively.

3.3. Admittance realization

The now fully-specified network can be realized with DVAs. For this, a MIMO relation between $\mathbf{V}_{out}$ and $\mathbf{V}_{in}$ can be prescribed with state-space models. Combining Equations (7), (10) and (20),

$$\begin{aligned}\boldsymbol{\Phi}_{in}^T\mathbf{V}_{in} &= \boldsymbol{\Phi}_{in}^T\mathbf{Z}_{DVA}(s)\mathbf{V}_{out}\\ &= \left(\boldsymbol{\Phi}_{in}^T\left(\mathbf{D}_{BD}+s\mathbf{Z}_{DVA}(s)\right)\boldsymbol{\Phi}_{out}-\boldsymbol{\Phi}_{in}^T\mathbf{D}_{BD}\boldsymbol{\Phi}_{out}\right)\boldsymbol{\eta}_e\\ &= \left(s^2\boldsymbol{\Omega}_e^{-2}+2s\mathbf{Z}_e\boldsymbol{\Omega}_e^{-1}+\mathbf{I}-\boldsymbol{\Phi}_{in}^T\mathbf{D}_{BD}\boldsymbol{\Phi}_{out}\right)\boldsymbol{\eta}_e.\end{aligned} \tag{45}$$

This system and Equation (10) are thus equivalent to the following state-space model

$$\begin{aligned}\begin{bmatrix}\dot{\boldsymbol{\eta}}_e\\ \ddot{\boldsymbol{\eta}}_e\end{bmatrix} &= \begin{bmatrix}\mathbf{0} & \mathbf{I}\\ -\boldsymbol{\Omega}_e^2\left(\mathbf{I}-\boldsymbol{\Phi}_{in}^T\mathbf{D}_{BD}\boldsymbol{\Phi}_{out}\right) & -2\boldsymbol{\Omega}_e\mathbf{Z}_e\end{bmatrix}\begin{bmatrix}\boldsymbol{\eta}_e\\ \dot{\boldsymbol{\eta}}_e\end{bmatrix}+\begin{bmatrix}\mathbf{0}\\ \boldsymbol{\Omega}_e^2\boldsymbol{\Phi}_{in}^T\end{bmatrix}\mathbf{V}_{in}\\ &= \mathbf{A}_e\begin{bmatrix}\boldsymbol{\eta}_e\\ \dot{\boldsymbol{\eta}}_e\end{bmatrix}+\mathbf{B}_e\mathbf{V}_{in},\\ \mathbf{V}_{out} &= \begin{bmatrix}\mathbf{0} & \boldsymbol{\Phi}_{out}\end{bmatrix}\begin{bmatrix}\boldsymbol{\eta}_e\\ \dot{\boldsymbol{\eta}}_e\end{bmatrix}=\mathbf{C}_e\begin{bmatrix}\boldsymbol{\eta}_e\\ \dot{\boldsymbol{\eta}}_e\end{bmatrix}.\end{aligned} \tag{46}$$

Owing to the block diagonal structure of every matrix used to build the state-space matrices in Equation (46), the latter have a block structure. Upon reordering the state variables, this block structure results into a block diagonal one. Hence, the state-space model can equivalently be built as the union of all state-space matrices built from Equation (46) using the group matrices $\mathbf{D}_e^{(g)}$, $\boldsymbol{\Omega}_e^{(g)}$, $\mathbf{Z}_e^{(g)}$, $\boldsymbol{\Phi}_{in}^{(g)}$ and $\boldsymbol{\Phi}_{out}^{(g)}$ in place of their global counterparts. This allows for a decentralized implementation of the networks, as expected. This realization is only possible thanks to the block diagonal structure of $\mathbf{D}_{BD}$. Had it been non-block-diagonal, either $\boldsymbol{\Phi}_{in}^T\mathbf{D}_{BD}\boldsymbol{\Phi}_{out}$ or $\boldsymbol{\Phi}_{in}$ and $\boldsymbol{\Phi}_{out}$ would also have had to lose that property, making a decentralized implementation impossible.

When the shunts and/or networks are to be emulated by digital units, an equivalent discrete state-space model can be obtained via Tustin's transform.

3.4. Summary of the tuning procedure

To end this section, the proposed tuning procedure is summarized. It goes as follows:

(i) Identify a model of the structure (Equation (5)): matrices $\boldsymbol{\Omega}_{oc}$, $\mathbf{B}$, $\mathbf{C}$ and $\mathbf{D}$.

(ii) Select the modes to be targeted and set the associated weights for each group $\mathbf{W}^{(g)}$.

(iii) For each group, determine the optimal input and output electrical mode shapes (Equations (30)-(37)).

(iv) For each targeted mode,

  (a) Compute the network's electromechanical coupling factors (Equations (24) and (39)).

  (b) Compute the optimal electrical resonance frequency (Equation (41)) and damping ratio (Equation (42)).

(c) Compute the electrical resonance frequency matrix (Equation (43)) and damping ratio matrix (Equation (44)).

(v) For each group, compute the state-space matrices (Equation (46)).

A more refined tuning procedure accounting for neglected effects was devised by the authors. The procedure is essentially similar to the one presented in this article, but brings corrections to the electrical resonance frequency and damping matrices in order to account for the effect of non-resonant modes [9] and sampling delays [39]. Owing to the rather technically involved character of this improved approach, it is detailed in the supplementary materials of this article. It should nonetheless be noted that the tuning approach explained therein is used in the examples in Sections 4 and 5. In general, accounting for non-resonant modes resulted in an improvement of maximum 1 dB in the attenuation in the cases studied in this work. This improvement could be more significant for more complex structures.

4. Performance comparison of centralized and decentralized absorbers

Using a fully centralized control approach may raise a series of practical issues. Since multiple transducers have to be controlled simultaneously, the DVA must have a sufficient number of inputs and outputs per digital unit, and computing power to handle the input-output relations in real time. If a network made up of passive elements were used, the large number of possible interconnections would potentially result in a large number electrical elements. A natural question is thus to ask what advantage the centralized approach has over the decentralized one.

Owing to the complexity of predicting the output of the SVDs necessary to compute the optimal electrical mode shapes in a general case, the discussion for multiple modes stays rather qualitative. General trends on performance of centralized and decentralized absorbers can nonetheless be deduced. Being understood that the discussion concerns a specific group, the superscript (g) is dropped in this section.

4.1. Single-mode case

When a single mode is considered, the dimensionless mode shape matrix reduces to a vector (i.e., $\boldsymbol{\Psi} = \boldsymbol{\psi}$) and the passivity constraint (Equation (38)) reduces to

$$1 - \boldsymbol{\psi}^T \boldsymbol{\psi} \geq 0, \tag{47}$$

i.e., $\boldsymbol{\psi}$ should be a unit vector. Using Equations (29) and (36), the optimal dimensionless electrical mode shape is

$$\boldsymbol{\psi}^\star = \arg \max_{\boldsymbol{\psi}} \frac{s_1 w_1}{\omega_{oc,r}} \mathbf{b}_r^T \mathbf{V}_D \boldsymbol{\Sigma}_D^{-1/2} \boldsymbol{\psi}. \tag{48}$$

Under its unitary constraint, it maximizes the objective function when it is aligned with $\mathbf{b}_r \mathbf{V}_D \boldsymbol{\Sigma}_D^{-1/2}$. This direction thus defines an optimal dimensionless mode shape that maximizes the MEMCF with mode r. This is similar to the principle used to tune

electrical analogs [21]: the electrical mode shapes should resemble those of the structure, as seen from the transducers.

Appendix A.3 demonstrates that decentralization has no effect on performance in this case. The network is thus equivalent to a set of RL circuits shunting each transducer individually and targeting the same mode. Intuitively, this result can be expected, because the full control capability of all transducers is focused on a single mode. In other words, the MEMCF of the *network* attains that of the *transducers*.

4.2. Multimodal case

When the shunts or networks target multiple modes, the passivity constraint expressed with dimensionless electrical mode shapes (Equation (38)) reads

$$\mathbf{I} - \mathbf{\Psi}^T\mathbf{\Psi} = \begin{bmatrix} 1-\boldsymbol{\psi}_1^T\boldsymbol{\psi}_1 & -\boldsymbol{\psi}_1^T\boldsymbol{\psi}_2 & \cdots & -\boldsymbol{\psi}_1^T\boldsymbol{\psi}_{N_e} \\ -\boldsymbol{\psi}_2^T\boldsymbol{\psi}_1 & 1-\boldsymbol{\psi}_2^T\boldsymbol{\psi}_2 & \cdots & -\boldsymbol{\psi}_2^T\boldsymbol{\psi}_{N_e} \\ \vdots & \vdots & \ddots & \vdots \\ -\boldsymbol{\psi}_{N_e}^T\boldsymbol{\psi}_1 & -\boldsymbol{\psi}_{N_e}^T\boldsymbol{\psi}_2 & \cdots & 1-\boldsymbol{\psi}_{N_e}^T\boldsymbol{\psi}_{N_e} \end{bmatrix} \succeq 0. \tag{49}$$

This matrix is positive semidefinite if and only if all of its principal minors are non-negative [40]. Considering the principal minors of order one (i.e., the diagonal elements), the following inequality for the k^{th} minor

$$1 - \boldsymbol{\psi}_k^T\boldsymbol{\psi}_k \geq 0 \tag{50}$$

must be satisfied. Similarly to the single mode case, this limits the norm of dimensionless mode shapes to one. Considering now minors of order two with rows k and l,

$$(1 - \boldsymbol{\psi}_k^T\boldsymbol{\psi}_k)(1 - \boldsymbol{\psi}_l^T\boldsymbol{\psi}_l) - (\boldsymbol{\psi}_k^T\boldsymbol{\psi}_l)^2 \geq 0, \tag{51}$$

which places further limits on the norms of these vectors if they are not orthogonal (i.e., when $\boldsymbol{\psi}_k^T\boldsymbol{\psi}_l \neq 0$). When possible, the SVD decomposition usually yields a family of orthogonal vectors $\mathbf{\Psi}$ to negate the influence of this constraint. This maximizes the norms of the dimensionless mode shapes and hence the electromechanical coupling.

When all optimal dimensionless mode shapes are orthogonal, a network that simultaneously attains optimal performance on each mode can be synthesized, i.e., the *network* attains the same MEMCFs as the *transducers* for all targeted modes. Following from the discussion in Section 4.1, this optimal performance would be observed individually on a specific mode if the set of transducers were connected to RL shunts targeting that mode. When this ideal case is not met, trade-offs have to be made between the controlled modes. The chosen weighting coefficients then set how the mode shapes align with their optimal counterparts, which directly affects the electromechanical coupling of the concerned modes (Equation (26)).

This electrical mode shapes optimization differs with the traditional electrical analog concept, and with the approach proposed in [28]. Indeed, in these approaches, the mode shapes are fixed equal to their single-mode optimal counterparts. Moreover, the dimensionless mode shapes orthogonality relates to the approach in [17], but the

method herein is more general and allows for the control of an arbitrary number of modes. From a control point of view, this corresponds to optimizing a set of gains between the transducers (which are used simultaneously as sensors and actuators) under the passivity constraint to maximize control authority.

We note that it is not possible to obtain a set of orthogonal dimensionless mode shapes when there are more modes to be controlled than transducers (because it is not possible to have N_e linearly independent vectors in a space of dimension N_p if $N_p < N_e$). Inherent performance limitations are thus to be expected in that case. This is more likely to happen when a decentralized approach is preferred over a centralized one, because the number of transducers per group N_p decreases. In particular, when there is a single transducer, $\boldsymbol{\Psi}$ is a $1 \times N_e$ vector. The matrix $\mathbf{I} - \boldsymbol{\Psi}^T\boldsymbol{\Psi}$ then admits $\boldsymbol{\Psi}^T$ as eigenvector with associated eigenvalue $1 - \boldsymbol{\Psi}\boldsymbol{\Psi}^T$. The other eigenvectors are orthogonal to $\boldsymbol{\Psi}^T$ and are associated to a unit eigenvalue. All eigenvalues are thus positive if $1 - \boldsymbol{\Psi}\boldsymbol{\Psi}^T \geq 0$, i.e.,

$$\sum_{n=1}^{N_e} \psi_n^2 \leq 1. \tag{52}$$

This passivity constraint is identical to that derived in [37] with Foster's reactance theorem. Specifically, the residues introduced therein correspond to squared modal amplitudes herein. It is also identical to the constraint imposed on the decentralized control approach obtained from the Youla parametrization of all stabilizing controllers proposed in [26].

Finally, it can be observed that a lack of orthogonality between the modes would result in a positive semidefinite matrix $\mathbf{I} - \boldsymbol{\Phi}_{in}^T \mathbf{D} \boldsymbol{\Phi}_{out}$. Equations (45) and (46) show that this matrix is associated with positive capacitive effects in the network. For shunts, it is known that positive capacitances negatively affect the electromechanical coupling [8, 11]. This gives another way to understand the adverse effects of the lack of orthogonality between the electrical modes.

In summary, optimal performance may be attained simultaneously on multiple modes if the associated optimal dimensionless mode shapes (which are characteristics of the host system) are orthogonal. Decentralization may have a detrimental effect on performance, especially if the optimal dimensionless mode shapes on the resulting subnetworks are not orthogonal. This is always the case when the number of targeted modes exceeds the number of transducers in the network, which is the case in particular for multi-resonant shunts. Trade-offs between the controlled modes then have to be made through the user-selected weighting coefficients. Since the upper bound for the subnetwork MEMCF is given by the MEMCF of its transducers, the latter also have to be selected according to the set of modes they should target.

4.3. A free-free piezoelectric beam

The free-free piezoelectric beam depicted in Figure 3 is considered herein to illustrate the effects of decentralization. It is excited by an external force at one end and its

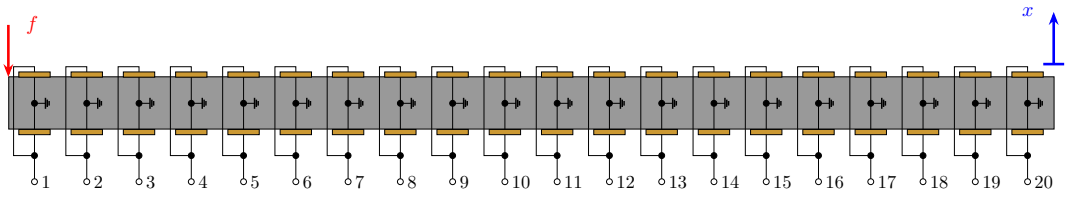

Figure 3: Schematic representation of the free-free piezoelectric beam [22].

response is measured at the other end. Details about this structure can be found in [22]. Twenty pairs of piezoelectric patches connected in parallel (each forming a piezoelectric cell) are distributed over the length of the structure and used to damp its first four bending modes. Similarly to [28], a finite element model of the beam was built using the procedure proposed by Thomas *et al* [30] with ten elements per cell. A model order reduction using the method in [41] was performed by retaining the excited mechanical and electrical degrees of freedom as well as twenty component normal modes. No damping was added to the host to focus on the effect of the proposed control approaches.

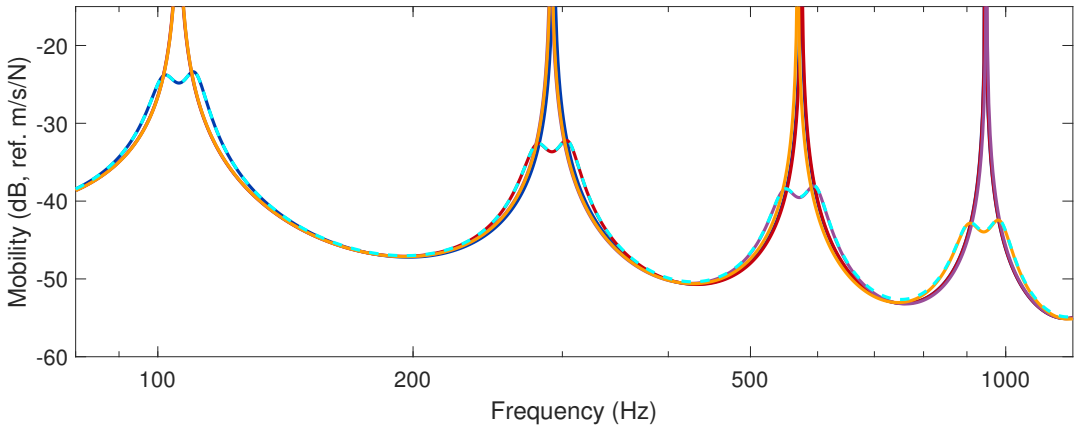

Figure 4: Mobility of the free-free beam with patches connected to individual series RL shunts, all targeting mode 1 (——), 2 (——), 3 (——) and 4 (——), and to a centralized network targeting the first four modes (- - - -).

4.3.1. Optimal performance of a fully centralized network The simultaneous optimal vibration reduction brought by a network on the first four bending modes is assessed. Figure 4 features the frequency response function (FRF) of the beam with a fully centralized network interconnecting the twenty patches and targeting the first four modes. Four other cases where all patches are individually shunted with single-mode series RL shunts, all targeting the same mode (one of the first four modes per case), are also displayed for comparison. For the network, identical unit weights were attributed to the four modes. Clearly, the network simultaneously attains the same performance on the four controlled modes as individual shunts focusing on a single mode, whereas

the latter produce nearly no attenuation on the non-targeted modes. This is possible because the modes of the beam are orthogonal, as seen from the twenty transducers. This illustrates the interest of centralization in terms of multimodal control.

Table 1: Modes targeted by the single-mode shunts for the free-free beam.

Patch	1	2	3	4	5	6	7	8	9	10	11	12	13	14	15	16	17	18	19	20
Mode	1	4	4	4	3	2	2	1	3	1	3	1	1	2	2	3	4	4	3	2

Table 2: Patches distribution among the groups in different cases for the free-free beam.

Patch	1	2	3	4	5	6	7	8	9	10	11	12	13	14	15	16	17	18	19	20
Shunts	1	2	3	4	5	6	7	8	9	10	11	12	13	14	15	16	17	18	19	20
Adjacent	1	1	1	1	1	2	2	2	2	2	3	3	3	3	3	4	4	4	4	4
Alternate	1	2	3	4	1	2	3	4	1	2	3	4	1	2	3	4	1	2	3	4
Centralized	1	1	1	1	1	1	1	1	1	1	1	1	1	1	1	1	1	1	1	1

4.3.2. Effect of decentralization The effects of decentralization are now investigated in terms of vibration reduction of the first four modes. Five cases are considered. The first two cases use individually-shunted patches with single-mode (series RL) or multi-resonant shunts. The mode distribution among the single-mode shunts (carried out manually to optimize and balance coupling with the targeted modes) is given in Table 1. We note that the multi-resonant shunts could be realized with classical circuits such as the current flowing or current blocking shunts [11] using the procedure described in [12]. The third and fourth cases consist in partially decentralized approaches, where four networks interconnect different sets of patches. In the third case, geometrically adjacent patches are grouped together, whereas in the fourth case, adjacent patches are alternatively distributed among the groups. The last case considers a fully centralized network interconnecting all patches. The patches distribution among the groups is detailed in Table 2. In all cases, each circuit or network targets the four modes with equal, unit weights on each mode.

Figure 5 presents the FRF of the beam for the five cases. As expected, the fully decentralized and centralized approaches result in the worst and best cases, respectively. The partially decentralized case with adjacent patch distribution features intermediate performance, while that with alternate distribution is identical to that of the fully centralized network. This shows that the patches distribution among the groups has a significant influence on performance. We also note that single-mode shunts outperform multi-resonant ones. This comes from the optimization of the modes distribution among the single-mode shunts. A better performance could be expected for multi-resonant shunts if the control weights were optimized as well, but this was not pursued here for

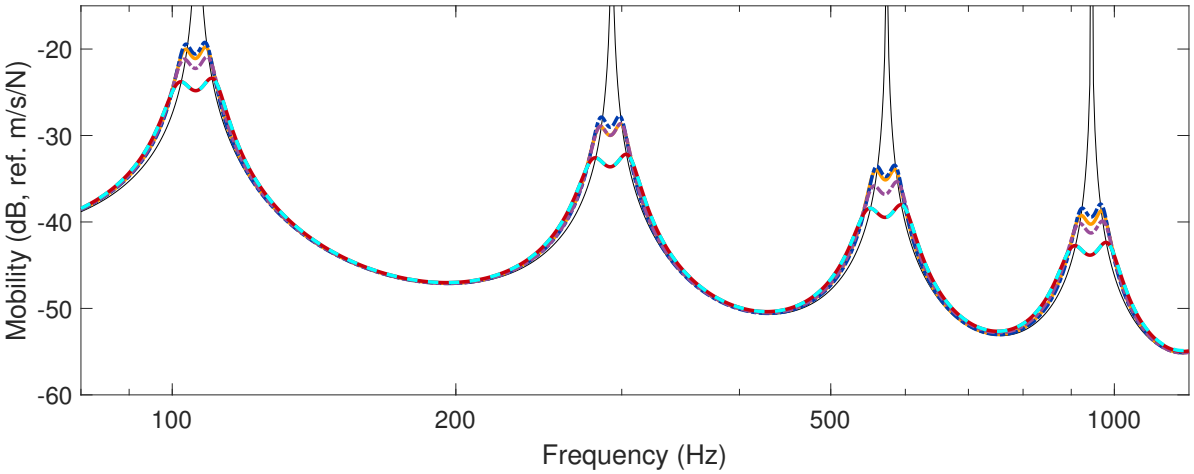

Figure 5: Mobility of the free-free beam with open-circuited patches (——), individual series RL shunts (——), individual multi-resonant shunts (— · —), four networks with adjacent (— · —) and alternate (——) distributions and a centralized network (- - - -) targeting the first four modes.

Table 3: Maximum amplitude of the free-free beam response in the vicinity of the targeted modes in different cases.

Mode	1	2	3	4
Shunts, single-mode	-19.8 dB	-28.7 dB	-33.9 dB	-38.7 dB
Shunts, multi-resonant	-19.2 dB	-27.7 dB	-33.4 dB	-37.9 dB
Adjacent	-20.9 dB	-28.6 dB	-35.3 dB	-39.9 dB
Alternate	-23.4 dB	-32.2 dB	-38.0 dB	-42.4 dB
Centralized	-23.4 dB	-32.2 dB	-38.0 dB	-42.4 dB

simplicity. The maximum amplitude in the vicinity of each targeted mode for each case is reported in Table 3.

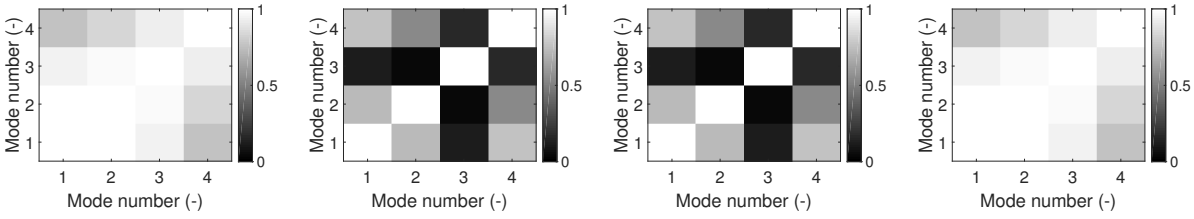

(a) (b) (c) (d)

Figure 6: AutoMAC matrix of the optimal electrical mode shapes for the groups with adjacent patches distribution: groups 1 (a), 2 (b), 3 (c) and 4 (d).

Further insight can be gained to understand the difference between the adjacent and alternate cases by looking at the optimal dimensionless electrical mode shapes orthogonality. To assess this, the auto modal assurance criterion (AutoMAC) matrix

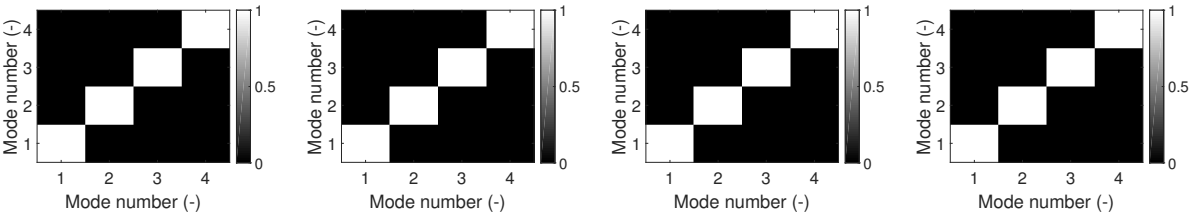

(a) (b) (c) (d)

Figure 7: AutoMAC matrix of the optimal electrical mode shapes for the groups with alternate patches distribution: groups 1 (a), 2 (b), 3 (c) and 4 (d).

whose entry (i, j) is defined by [24, 42]

$$(\text{AutoMAC})_{ij} = \frac{\left((\boldsymbol{\psi}_i^\star)^T \boldsymbol{\psi}_j^\star\right)^2}{||\boldsymbol{\psi}_i^\star||^2||\boldsymbol{\psi}_j^\star||^2} = \left((\boldsymbol{\psi}_i^\star)^T \boldsymbol{\psi}_j^\star\right)^2 \tag{53}$$

can be used. The values that this entry can take range from zero to one; a value of zero for a non-diagonal entry indicates near-orthogonality between the associated modes. The AutoMAC matrices are featured in Figures 6 and 7 for the adjacent and alternate distributions, respectively. Clearly, the alternate distribution features much better (almost perfect) orthogonality, allowing the passive networks to attain optimal performance on all controlled modes simultaneously. By contrast, the adjacent distribution performance is hindered by the lack of orthogonality of the optimal electrical mode shapes.

5. A clamped-free piezoelectric beam

The theoretical developments are numerically and experimentally illustrated on a clamped-free piezoelectric beam in this section.

5.1. Numerical verification

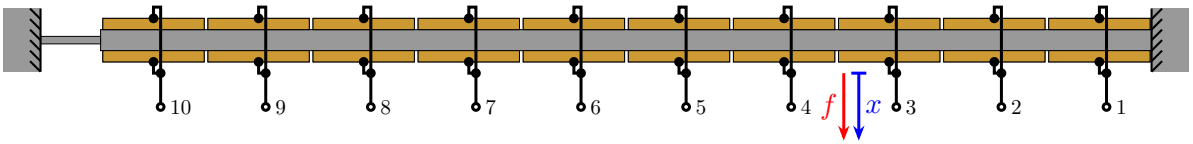

Figure 8: Schematic representation of the clamped-free piezoelectric beam with a thin lamina.

The 70 cm long clamped-free beam with an attached thin lamina depicted in Figure 8 is now considered. Ten pairs of piezoelectric patches connected in parallel (each forming a piezoelectric cell) are distributed over the length of the beam. Details about this structure can be found in [12, 25]. We note that the thin lamina can be

Table 4: Numerical characteristics of the clamped-free piezoelectric beam with five equivalent transducers (parallel connection of cells (1,2), (3,4), (5,6), (7,8) and (9,10)).

Mode	1	2	3	4
f_{oc} (Hz)	33	158	435	846
$K_c^{(1)}$ (-)	0.13	0.095	0.045	0.003
$K_c^{(2)}$ (-)	0.081	0.055	0.106	0.056
$K_c^{(3)}$ (-)	0.037	0.126	0.005	0.105
$K_c^{(4)}$ (-)	0.005	0.093	0.12	0.065
$K_c^{(5)}$ (-)	0.006	0.019	0.046	0.07

responsible for a nonlinear structural behavior [25], but the forcing levels considered in this study are kept low enough to make this effect negligible.

The beam is excited 20 cm away from its clamped end, and its collocated displacement is monitored to assess the performance of the different control approaches. Similarly to [12], a finite element model of the beam was built with one element per millimeter and reduced by retaining the excited mechanical and electrical degrees of freedom as well as twenty component normal modes [30, 41]. Modal damping of 0.2% was added on each mode to simulate approximately the experimental results.

In order to replicate the experimental setup considered in Section 5.2.5, all piezoelectric cells are connected in parallel by adjacent pairs $(2i-1, 2i)$ with $i = 1, \cdots, 5$, forming five equivalent transducers (which are ordered starting from the clamped end). The characteristics of the beam are reported in Table 4. In this table, $f_{oc} = \omega_{oc}/(2\pi)$ is the resonance frequency of the structure with all equivalent transducers in open circuit, and $K_c^{(p)}$ is evaluated with Equation (39) for the equivalent transducer p.

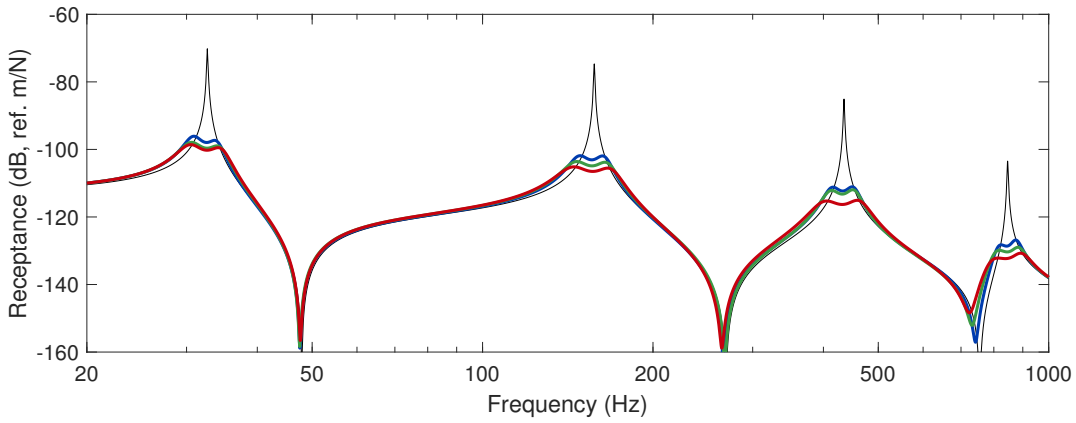

Figure 9: Numerical receptance of the clamped-free beam with five equivalent transducers in open circuit (——), connected to a network (——), three decentralized networks (——) or five shunts (——) targeting the first four modes.

Figure 9 presents the receptance of the beam controlled with different approaches.

Table 5: Maximum voltages and currents of the absorbers under a harmonic external forcing for the clamped-free beam.

Equivalent transducer	1	2	3	4	5
Maximum voltage, shunts (V/N)	22.15	8.62	13.68	7.98	3.14
Maximum current, shunts (mA/N)	0.48	1.27	1.30	2.01	1.66
Maximum voltage, partially decentralized (V/N)	19.80	14.05	11.57	8.33	1.87
Maximum current, partially decentralized (mA/N)	0.56	1.34	1.35	1.82	0.97
Maximum voltage, centralized (V/N)	19.64	12.30	10.00	7.44	1.98
Maximum current, centralized (mA/N)	0.77	1.52	1.23	1.60	0.83

In addition to the fully centralized and decentralized cases, a partially decentralized case was investigated, grouping the equivalent transducers 1 and 2, as well as 3 and 4, while leaving transducer 5 individually shunted. The three approaches are thus similar to the three cases depicted in Figure 2. In all cases, weights $w_1 = 1$, $w_2 = 0.88$, $w_3 = 0.71$ and $w_4 = 0.77$ were empirically attributed to the four modes to obtain a somewhat balanced reduction of about 30 dB for each mode. Again, all approaches feature effective vibration mitigation of the targeted modes. The fully decentralized, partially decentralized and fully centralized approaches rank from worst to best in terms of performance.

To have an idea of the control effort in each case, Table 5 gathers the maximum voltages and currents of each transducer under a harmonic external forcing. Furthermore, the maximum voltage can be used as a design criterion to choose the electronic components of the DVA and the supply voltage. Finally, this supply voltage and the maximum current can be used to estimate the power consumption of the DVA [41].

5.2. Experimental validation

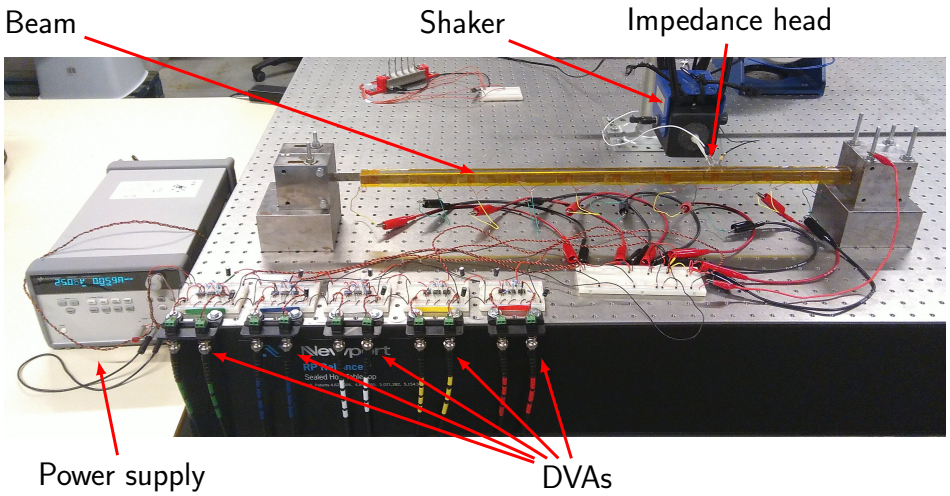

Figure 10: Picture of the experimental setup.

Table 6: Experimental damping ratios of the clamped-free piezoelectric beam.

Mode	1	2	3	4
Damping ratio (-)	0.0030	0.0015	0.0022	0.0063

Table 7: Experimental characteristics of the clamped-free piezoelectric beam with two equivalent transducers (parallel connection of cells (1,2) and (4,5)).

Mode	1	2	3
f_{oc} (Hz)	33	146	383
$K_c^{(1)}$ (-)	0.091	0.059	0.008
$K_c^{(2)}$ (-)	0.046	0.092	0.05

The beam whose numerical model was studied in Section 5.1 was used to experimentally validate the proposed approach. Figure 10 shows a picture of the experimental setup. The beam was excited with an electrodynamic shaker 20 cm away from its clamped end. The force applied on the structure and its collocated acceleration were measured by an impedance head. Different sets of patches were connected to custom-made DVAs. These DVAs were realized by connecting a dSPACE MicroLabBox controller to up to five custom-made analog circuits containing a voltage sensor and a current injector. Details about the analog circuits are given in Appendix B. The sampling frequency of the digital unit was set to 50 kHz, i.e., more than 50 times higher than the highest frequency of the controlled modes. Yet, the effect of delays was observable and a procedure to counteract this, based on the approach proposed in [39], was used (which is also detailed in the supplementary materials of this article).

The characteristics of the host system were measured using DVAs only. A set of pseudorandom excitation currents were injected into the patches, and their voltages were recorded. Estimates of the matrices in Equations (6) were then derived using the PolyMAX identification method [34]. Damping ratios of 0.1 to 0.6% were identified for the first four bending modes of the uncontrolled structure, as reported in Table 6.

5.2.1. Control of two modes with two transducers The first two bending modes of the beam were targeted to begin with. To simultaneously maximize and balance the control authority over these two modes, two equivalent transducers, composed of the parallel connection of cells (1,2) and (4,5) were used. These connections were chosen based on a study of the numerical model to maximize coupling with the two first modes with two equivalent transducers. Table 7 reports the experimental characteristics identified with the PolyMAX method for the system under this configuration.

Figure 11 features experimental frequency response functions (FRFs) of the beam with transducers in open circuit or connected to shunts or a network. For these two latter cases, weights $w_1 = 1.2$ and $w_2 = 1$ were attributed to the first and second mode,

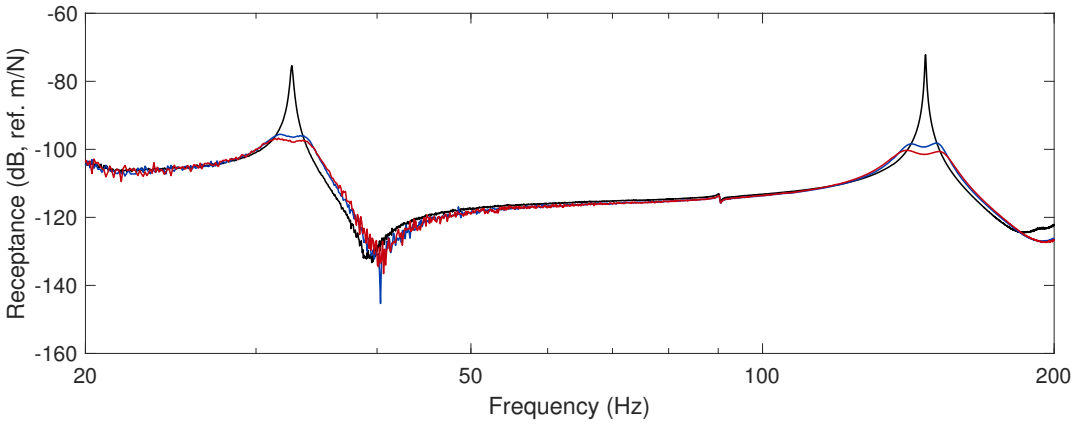

Figure 11: Experimental receptance of the clamped-free beam with two equivalent transducers in open circuit (——), connected to shunts (——) or a network (——) targeting the first two modes with $w_1/w_2 = 1.2$.

respectively. The two targeted resonances are effectively mitigated by both approaches. A slightly better performance in terms of amplitude reduction is obtained with networks.

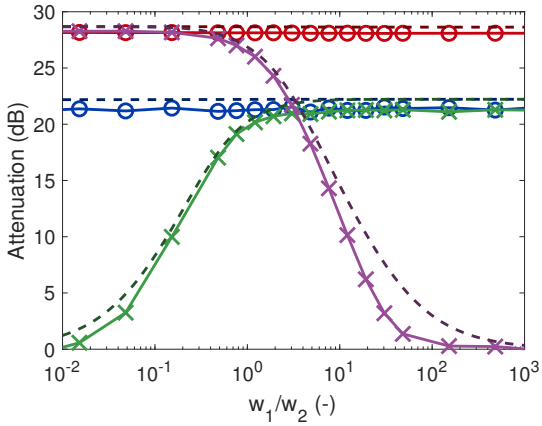

Figure 12: Attenuations on the targeted modes of the clamped-free beam as functions of the weights ratio: network (—— : mode 1, —— : mode 2; −∘−: experimental, - - - -: theoretical [36]) and shunts (—— : mode 1, —— : mode 2; −×−: experimental, - - - -: theoretical [36]).

A more thorough investigation of the effect of the chosen control weights is reported in Figure 12. FRFs of the controlled beam were measured for $w_2 = 1$ and various values of w_1. All these FRFs are not disclosed here for brevity, but the attenuation on each mode (defined as the ratio of the maximum amplitude of the open-circuit FRF to that of the controlled FRF) is shown. A striking difference is observable between networks and shunts: while the former are almost insensitive to the weight ratio w_1/w_2, the latter clearly prioritize the mode with the highest weight at the expense of attenuation on the other, which highlights the trade-off mentioned in Section 4.2. The networks insensitivity can be explained by the near perfect orthogonality of the optimal

dimensionless mode shapes in this setup.

The experimental attenuations can be compared to those which would theoretically be expected. Based on the model given in Equation (21) and using the MEMCF given by Equation (26) and the damping ratios evaluated from the open-circuit FRF, a formula from Thomas *et al* [36] allows for the prediction of the attenuation, similarly to what was done in [37]. As shown in Figure 12, there is a remarkable quantitative agreement between the theoretical and experimental results. The respective sensitivity and insensitivity of the shunts and networks to the weight ratio is clearly reproduced. A slight disagreement can be observed between theory and experiments for shunts on mode 2 around $w_1/w_2 = 50$. This can be explained by the fact that the frequency of this mode was slightly underestimated, leading to an imperfect tuning of the resonant shunts during this study. This is more significant for small weights on mode 2 (see, e.g., Figure 15 hereafter).

5.2.2. Robustness against frequency variations Resonant absorbers are an effective solution for vibration mitigation, yet they are also known for lacking robustness [43]. To assess this, uncertainty in the host structure parameters was simulated by changing the identified parameters, and using these modified parameters in the absorbers tuning.

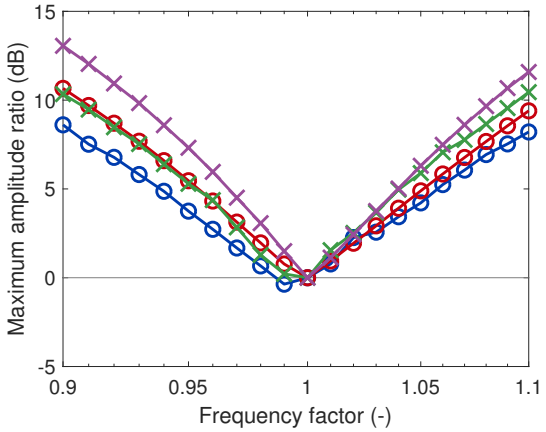

Figure 13: Ratio of the maximum of the experimental FRF amplitude of the clamped-free beam in the detuned case to that in the tuned case of the network (−○− : mode 1, −○− : mode 2) and shunts (−×− : mode 1, −×− : mode 2) under frequency variations of the DVAs.

At first, a factor was applied to the identified frequencies of the first two modes, thereby detuning the absorbers, while setting $w_1 = 1.2$ and $w_2 = 1$. Figure 13 features the effect of such a detuning on performance for both control approaches. For a fair comparison, the maximum amplitude of the FRF around the targeted mode for a detuned case was divided by that of the tuned case. It can be observed that the tuned case, where the frequency factor is equal to one, is optimal or nearly-optimal. Underestimation or overestimation of the frequencies generally lead to a deterioration

of the attenuation. This trend is qualitatively similar for shunts and networks owing to their resonant nature, similarly to what was observed in [29]. Networks are slightly more robust than shunts because of their higher electromechanical coupling with the targeted modes [43].

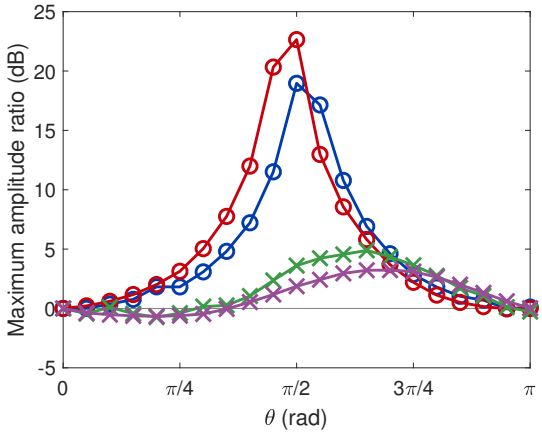

Figure 14: Ratio of the maximum of the experimental FRF amplitude of the clamped-free beam in the detuned case to that in the tuned case of the network (−○− : mode 1, −○− : mode 2) and shunts (−×− : mode 1, −×− : mode 2) under mode shapes variations of the DVAs.

5.2.3. Robustness against mode shapes variations A second series of robustness tests was performed to assess the dependency of performance on the identified mode shapes. To achieve this, the optimal input and output mode shapes were rotated by an angle θ to yield their detuned counterparts $\widetilde{\boldsymbol{\Phi}}_{in}$ and $\widetilde{\boldsymbol{\Phi}}_{out}$ as

$$\widetilde{\boldsymbol{\Phi}}_{in} = \boldsymbol{\Phi}_{in} \begin{bmatrix} \cos(\theta) & -\sin(\theta) \\ \sin(\theta) & \cos(\theta) \end{bmatrix}, \qquad \widetilde{\boldsymbol{\Phi}}_{out} = \boldsymbol{\Phi}_{out} \begin{bmatrix} \cos(\theta) & -\sin(\theta) \\ \sin(\theta) & \cos(\theta) \end{bmatrix}, \tag{54}$$

respectively. The values $\theta = 0$ and $\theta = \pi$ correspond to the tuned case, and intermediate values represent a detuning in the mode shapes. Figure 14 presents the effect of such a rotation on performance. While shunts are mildly affected, networks feature a strong dependency on a correct tuning of the mode shapes, the tuned case being the optimal one. The case where $\theta = \pi/2$ makes the detuned electrical resonant mode shapes orthogonal to their tuned counterparts. This results in nearly no coupling, and consequently nearly no attenuation on the targeted modes. Networks thus appear to be more sensitive than shunts to mode shapes uncertainties. It should nonetheless be noted that the worst case $\theta = \pi/2$ corresponds to swapping the mode shapes of modes 1 and 2, which constitutes a huge error that is very unlikely to occur in practice.

5.2.4. Control of three modes with two transducers To highlight the limitations of networks controlling more modes than their number of transducers, a case with two transducers (identical to those of the previous case) used to mitigate the first three

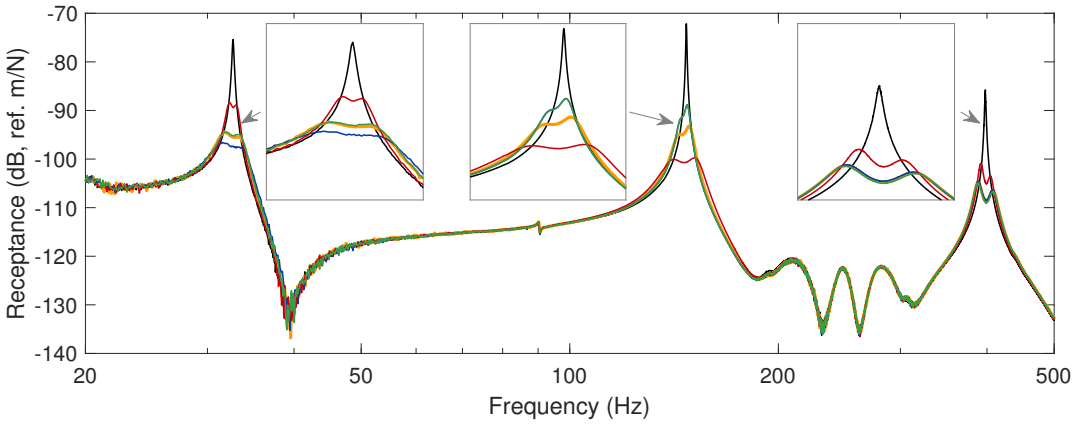

(a)

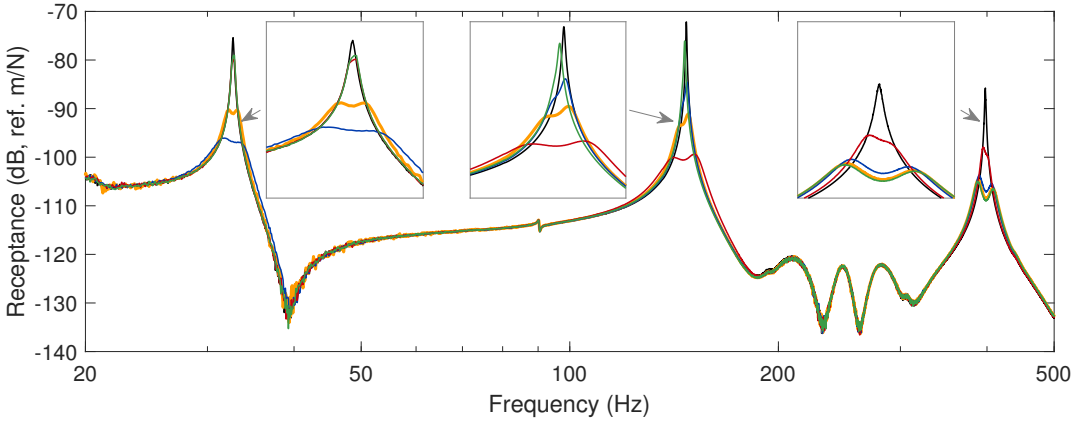

(b)

Figure 15: Experimental receptance of the clamped-free beam with two equivalent transducers in open circuit (——), connected to a network (a) or shunts (b) targeting the first three modes: baseline case (——), and emphasis on modes 1 (——), 2 (——) and 3 (——).

bending modes is considered next. Figure 15 presents FRFs of the beam controlled with networks and multi-resonant shunts. Between the second and third bending modes, a dynamic phenomenon appears in place of an expected antiresonance (around 250 Hz). This feature could be attributed to a shaker-structure interaction, because it was observed to be quite sensitive to the shaker and stinger positions. Another reason could be the non-ideal, dynamic characteristics of the clamping. A detailed investigation was not carried out since this occurs at low amplitudes anyways.

A baseline case was empirically selected with $w_1 = 0.1$, $w_2 = 0.2$ and $w_3 = 1.7$ to obtain a somewhat balanced reduction on all targeted modes. Emphasis on a specific mode was then sought by multiplying the corresponding weight by ten while keeping the weights associated with other modes to their baseline value. In contrast to the case with two modes, a trade-off in performance is observable with networks, i.e., an increased vibration reduction on a mode comes at the expense of reduced vibration reduction on other modes, in accordance with the discussion in Section 4. The concessions that

Table 8: Maximum experimental amplitude of the clamped-free beam response in the vicinity of the targeted modes in different cases.

Mode	1	2	3
Open circuit	-75.4 dB	-72.2 dB	-85.8 dB
Shunts, baseline	-94.4 dB	-93.2 dB	-104.7 dB
Shunts, mode 1	-96.6 dB	-88.8 dB	-104.6 dB
Shunts, mode 2	-88.4 dB	-99.7 dB	-100.9 dB
Shunts, mode 3	-94.4 dB	-88.8 dB	-104.9 dB
Network, baseline	-90.3 dB	-91.1 dB	-104.8 dB
Network, mode 1	-96.1 dB	-84.5 dB	-103.7 dB
Network, mode 2	-79.9 dB	-99.4 dB	-97.9 dB
Network, mode 3	-79.0 dB	-76.1 dB	-105.0 dB

Table 9: Experimental characteristics of the clamped-free piezoelectric beam with five equivalent transducers (parallel connection of cells (1,2), (3,4), (5,6), (7,8) and (9,10)).

Mode	1	2	3	4
f_{oc} (Hz)	33	146	381	811
$K_c^{(1)}$ (-)	0.093	0.059	0.009	0.02
$K_c^{(2)}$ (-)	0.069	0.057	0.092	0.046
$K_c^{(3)}$ (-)	0.027	0.102	0.021	0.079
$K_c^{(4)}$ (-)	0	0.079	0.105	0.059
$K_c^{(5)}$ (-)	0.006	0.015	0.036	0.058

have to be made by shunts are nonetheless much more stringent, and in some cases the amplitude of the non-emphasized modes is barely reduced compared to the uncontrolled case. Table 8 summarizes the maximum amplitude in the vicinity of the controlled modes.

5.2.5. Control of four modes with five transducers A final case is investigated to demonstrate the control of the first four bending modes (i.e., all bending modes below 1000 Hz). All piezoelectric cells are connected in parallel by adjacent pairs $(2i-1, 2i)$ with $i = 1, \cdots, 5$, forming five equivalent transducers. The characteristics identified thanks to the PolyMAX method are reported in Table 9. Comparing these experimental results with the numerical ones (Table 4), we note first that the frequencies of the highest modes in the numerical model tend to be overestimated. This can mainly be attributed to an imperfect clamping of finite stiffness. As similarly noted in [25], the overall electromechanical coupling is also overestimated in the numerical model. This discrepancy can most probably be attributed to neglected 3D piezoelectric effects [44], as well as imperfect bonding between the patches and the beam. Nevertheless, since the proposed method does not rely on the numerical model but rather on the identified one,

these discrepancies do not affect the effectiveness of the different control approaches.

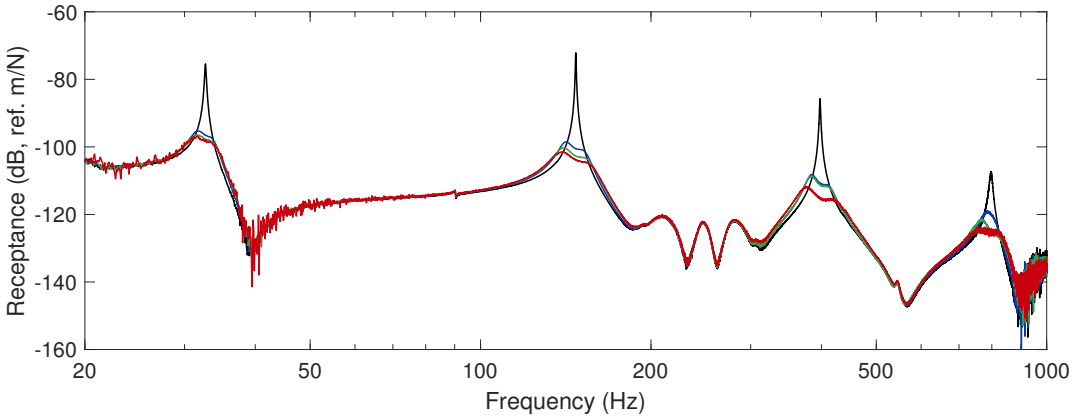

Figure 16: Experimental receptance of the beam with five equivalent transducers in open circuit (——), connected to a network (——), three decentralized networks (——) or five shunts (——) targeting the first four modes.

Figure 16 features FRFs with groups shunted individually or interconnected via networks. Weights $w_1 = 1$, $w_2 = 0.88$, $w_3 = 0.71$ and $w_4 = 0.77$ were selected to replicate the numerical results with the centralization pattern depicted in Figure 2. As expected, the fully centralized network offers the best performance, followed by the partially decentralized case as an intermediate solution and finally by the shunts. A strong qualitative similarity between Figures 9 and 16 is observed. Quantitatively, the reductions predicted by the numerical model overestimate the experimental ones, which is in direct link with the electromechanical coupling overestimation.

6. Conclusion

Shunts and networks can be used alike for effective multimodal vibration mitigation of structures with multiple piezoelectric transducers. A unified modeling framework and tuning procedure for these control approaches were proposed in this work. The dynamic characteristics of passive resonant controllers were optimized to provide effective multimodal damping. The implications of decentralization on performance were also discussed, and it was shown that networks generally outperform shunts if multiple modes are targeted. Both types of control approaches feature similar robustness against frequency detuning, but networks are more sensitive to mode shapes misestimation.

DVAs were leveraged to realize the shunts and networks. The proposed tuning approach was developed using characteristics that can be directly identified from these DVAs. It was numerically verified on free-free and clamped-free beams, and experimentally validated on a clamped-free beam. In all cases, the effectiveness of the different methods was demonstrated and compared.

This work could have several potentially interesting extensions. First, a more thorough investigation of the distribution of the modes to be controlled among the

different transducers could be carried out. A procedure including the transducers' positions, sizes and materials as optimization variables would be another interesting extension to this work. The objective function could account for these parameters, but the optimization problem would most likely require an iterative procedure. A simplified identification procedure of the system could also be devised, in order to potentially allow for a fully embedded approach, where the DVAs would be able to autonomously tune themselves to control the host structure. Finally, network synthesis techniques could be used to find actual passive electrical elements to build up the designed shunts or networks, thereby resulting in a fully passive control solution.

Acknowledgments

Ghislain Raze is a Postdoctoral Researcher of the Fonds de la Recherche Scientifique - FNRS which is gratefully acknowledged. The authors would also like to acknowledge the financial support of the SPW (WALInnov grant 1610122).

Appendix A. Mathematical proofs

Appendix A.1. Passivity constraints

The case where the piezoelectric transducers are connected to a purely passive network is considered as a reference. This case corresponds to $\mathbf{G}_{in} = \mathbf{G}_{out} = \mathbf{I}$. The charges and voltages of the transducers are related by

$$\mathbf{V}_p = s\mathbf{Z}_n(s)\mathbf{q}_p, \tag{A.1}$$

where $\mathbf{Z}_n$ is the impedance matrix of the network. To respect the reciprocity principle, the input and output mode shapes have to be equal. Setting them to $\mathbf{\Phi}_p$, Equation (9) becomes

$$\mathbf{\Phi}_p^T \left(\mathbf{E}_p^\varepsilon + s\mathbf{Z}_n(s)\right) \mathbf{\Phi}_p = s^2\mathbf{\Omega}_e^{-2} + 2s\mathbf{Z}_e\mathbf{\Omega}_e^{-1} + \mathbf{I}, \tag{A.2}$$

(where in this case $\mathbf{D}$ and $\mathbf{E}_p^\varepsilon$ are equal owing to Equation (6)). According to Gannett and Chua [45], the matrix $\mathbf{Z}_n$ must fulfill the conditions

(i) $\mathbf{Z}_n(s)$ has no poles in $\{s \in \mathbb{C} | \Re(s) > 0\}$ ($\Re$ denotes the real part operator),

(ii) $\mathbf{Z}_n(\sigma)$ is a real matrix for $\sigma \in \mathbb{R}^+$,

(iii) $\mathbf{Z}_n(s) + \mathbf{Z}_n^H(s)$ is positive semidefinite in $\{s \in \mathbb{C} | \Re(s) > 0\}$ (superscript H denotes Hermitian transposition),

(iv) the network associated to $\mathbf{Z}_n$ is controllable,

in order to be the impedance matrix of a passive network. Conditions (i) and (ii) are verified as long as the electrical mode shapes, frequencies and damping ratios are real, and condition (iv) is verified as long as $\mathbf{\Phi}_p$ is full column rank. Condition (iii) requires further developments to be checked. In this regard, the inequality featured in

condition (iii) is projected onto the subspace spanned by $\mathbf{\Phi}_p$ and Equation (A.2) is used to yield

$$\begin{aligned}&\mathbf{\Phi}_p^T \left(\mathbf{Z}_n(s) + \mathbf{Z}_n^H(s)\right) \mathbf{\Phi}_p \\ &= (s + s^*)\, \mathbf{\Omega}_e^{-2} + 4\mathbf{Z}_e\mathbf{\Omega}_e^{-1} + \left(\tfrac{1}{s} + \tfrac{1}{s^*}\right) \left(\mathbf{I} - \mathbf{\Phi}_p^T \mathbf{E}_p^{\varepsilon} \mathbf{\Phi}_p\right) \succeq 0 \qquad \forall s \in \mathbb{C} | \Re(s) > 0,\end{aligned} \tag{A.3}$$

where superscript $*$ denotes complex conjugation. A sufficient condition to satisfy this inequality is to guarantee the positive semidefiniteness of matrices associated with each power of s. For the matrices associated with s^1 and s^0, this implies that the electrical frequencies and damping ratios must be positive. For the one associated with s^{-1}, the passivity condition reduces to

$$\mathbf{I} - \mathbf{\Phi}_p^T \mathbf{E}_p^{\varepsilon} \mathbf{\Phi}_p \succeq 0. \tag{A.4}$$

If the rank of $\mathbf{\Phi}_p$ is equal to N_p, Equation (A.3) fully constrains the impedance matrix of the network. In the opposite case, there exists a non-empty set of orthogonal vectors $\mathbf{N}_p$ such that $\mathbf{\Phi}_p^T \mathbf{N}_p = \mathbf{0}$. Then, to fully satisfy condition (iii), Equation (A.3) needs to be complemented by

$$\mathbf{N}_p^T \left(\mathbf{Z}_n(s) + \mathbf{Z}_n^H(s)\right) \mathbf{N}_p \succeq 0 \qquad \forall s \in \mathbb{C} | \Re(s) > 0. \tag{A.5}$$

Equation (9) does not impose any constraint on this subspace, leaving some freedom in the design. The impedance matrix can thus be chosen to have $\mathbf{N}_p$ as null space as well for simplicity.

Considering now the case where $\mathbf{G}_{in} \neq \mathbf{I}$ and $\mathbf{G}_{out} \neq \mathbf{I}$, it is aimed to make $\mathbf{Z}_{DVA}$ have an identical effect to the passive network characterized by $\mathbf{Z}_n$. From Equations (4) and (A.1), these impedance matrices are related by

$$\mathbf{Z}_{DVA}(s) = \mathbf{G}_{out} \mathbf{Z}_n(s) \mathbf{G}_{in}. \tag{A.6}$$

With this relation, equating Equations (9) and (A.2) shows that the electrical mode shapes $\mathbf{\Phi}_{in}$ and $\mathbf{\Phi}_{out}$ must be constrained to satisfy the reciprocity condition

$$\mathbf{G}_{out} \mathbf{\Phi}_{out} = \mathbf{G}_{in}^T \mathbf{\Phi}_{in} = \mathbf{\Phi}_p. \tag{A.7}$$

Multiplying Equation (A.7) by $\mathbf{\Theta}$ and using Equation (6), one gets Equation (12). Then, using Equations (6) and (A.7), Equation (A.4) turns to Equation (13).

The positive character of the (real) electrical resonance frequencies and damping ratios, the full rank condition on $\mathbf{\Phi}_{in}$, as well as Equations (12) and (13) thus form sufficient conditions to ensure the passivity of the emulated circuit or network.

Appendix A.2. Optimal electrical mode shapes

The terminology of Ten Berge [46] is used in this section. With the SVD of $\mathbf{D}$ (Equation (30)), Equation (13) becomes

$$\mathbf{I} - \mathbf{\Phi}_{in}^T \mathbf{U}_D \mathbf{\Sigma}_D \mathbf{V}_D^T \mathbf{\Phi}_{out} \succeq 0. \tag{A.8}$$

Introducing the normalized mode shape matrix $\mathbf{\Psi}$ and diagonal scaling matrix $\mathbf{S}$ such that

$$\mathbf{\Phi}_{in} = \mathbf{U}_D \mathbf{\Sigma}_D^{-1/2} \mathbf{\Psi} \mathbf{S}^{-1} \tag{A.9}$$

$$\mathbf{\Phi}_{out} = \mathbf{V}_D \mathbf{\Sigma}_D^{-1/2} \mathbf{\Psi} \mathbf{S}, \tag{A.10}$$

Equation (A.8) becomes

$$\mathbf{I} - \mathbf{S}^{-1} \mathbf{\Psi}^T \mathbf{\Psi} \mathbf{S} \succeq 0. \tag{A.11}$$

This inequality is equivalent, up to a regular similarity transformation with the matrix $\mathbf{S}$, to

$$\mathbf{I} - \mathbf{\Psi}^T \mathbf{\Psi} \succeq 0. \tag{A.12}$$

This inequality is satisfied if the eigenvalues of $\mathbf{\Psi}^T \mathbf{\Psi}$, i.e., the singular values of $\mathbf{\Psi}$ squared, are less than or equal to one. One thus deduces that $\mathbf{\Psi}$ must be suborthonormal [46]. The set of suborthonormal matrices of arbitrary size is noted $\mathbb{S}$. Using Equations (28) and (A.10), the optimization problem then becomes

$$\max_{\mathbf{\Psi} \in \mathbb{S}} \operatorname{Tr}\left(\mathbf{W} \mathbf{\Omega}_{oc}^{-1} \mathbf{B} \mathbf{V}_D \mathbf{\Sigma}_D^{-1/2} \mathbf{\Psi} \mathbf{S} \right) = \max_{\mathbf{\Psi} \in \mathbb{S}} \operatorname{Tr}\left(\mathbf{S} \mathbf{W} \mathbf{\Omega}_{oc}^{-1} \mathbf{B} \mathbf{V}_D \mathbf{\Sigma}_D^{-1/2} \mathbf{\Psi} \right). \tag{A.13}$$

We note that the latter equality, which follows from the trace properties, could also have been derived from the fact that matrices $\mathbf{B}$ and $\mathbf{C}$ are unique up to a multiplication by a diagonal matrix. At this point, both $\mathbf{\Psi}$ and $\mathbf{S}$ are unknown. An optimal $\mathbf{\Psi}$ shall first be determined as an implicit function of $\mathbf{S}$, which can be derived afterward. It is now assumed that the matrix premultiplying $\mathbf{\Psi}$ admits a compact SVD decomposition given by Equation (34) ("compact" meaning here that $\mathbf{\Sigma}_M$ is a square matrix containing only the non-zero singular values), leading to

$$\max_{\mathbf{\Psi} \in \mathbb{S}} \operatorname{Tr}\left(\mathbf{S} \mathbf{W} \mathbf{\Omega}_{oc}^{-1} \mathbf{B} \mathbf{V}_D \mathbf{\Sigma}_D^{-1/2} \mathbf{\Psi} \right) = \max_{\mathbf{\Psi} \in \mathbb{S}} \operatorname{Tr}\left(\mathbf{U}_M \mathbf{\Sigma}_M \mathbf{V}_M^T \mathbf{\Psi} \right). \tag{A.14}$$

The suborthonormal matrix $\mathbf{\Psi}$ can be assumed to be the product of two suborthonormal matrices $\mathbf{P}$ and $\mathbf{Q}$ as

$$\mathbf{\Psi} = \mathbf{P} \mathbf{Q}^T, \tag{A.15}$$

transforming the optimization problem to

$$\max_{\mathbf{P},\mathbf{Q} \in \mathbb{S}} \operatorname{Tr}\left(\mathbf{U}_M \mathbf{\Sigma}_M \mathbf{V}_M^T \mathbf{P} \mathbf{Q}^T \right) = \max_{\mathbf{P},\mathbf{Q} \in \mathbb{S}} \operatorname{Tr}\left(\mathbf{Q}^T \mathbf{U}_M \mathbf{\Sigma}_M \mathbf{V}_M^T \mathbf{P} \mathbf{I} \right). \tag{A.16}$$

Matrices $\mathbf{Q}^T \mathbf{U}_M$ and $\mathbf{V}_M^T \mathbf{P}$ are suborthonormal, while matrices $\mathbf{\Sigma}_M$ and $\mathbf{I}$ are diagonal with positive elements. Therefore, Ten Berge's theorem [46] can be called upon to show that the objective function is bounded by

$$\operatorname*{Tr}_{\mathbf{P},\mathbf{Q} \in \mathbb{S}} \left(\mathbf{Q}^T \mathbf{U}_M \mathbf{\Sigma}_M \mathbf{V}_M^T \mathbf{P} \mathbf{I} \right) \leq \operatorname{Tr}\left(\mathbf{\Sigma}_M \mathbf{I} \right) = \operatorname{Tr}\left(\mathbf{\Sigma}_M \right). \tag{A.17}$$

This maximum is reached, i.a., when $\mathbf{Q}^T \mathbf{U}_M = \mathbf{I}$ and $\mathbf{V}_M^T \mathbf{P} = \mathbf{I}$. Given the semi-orthonormal character of the matrices $\mathbf{U}_M$ and $\mathbf{V}_M$ ($\mathbf{U}_M^T \mathbf{U}_M = \mathbf{I}$ and $\mathbf{V}_M^T \mathbf{V}_M = \mathbf{I}$), it is thus deduced that $\mathbf{Q} = \mathbf{U}_M$ and $\mathbf{P} = \mathbf{V}_M$ constitute a (non-unique) optimal

choice. Finally, injecting this result into Equation (A.15) and back into Equations (A.9) and (A.10), one obtains Equations (35) and (36).

Ten Berge's inequality (Equation (A.17)) somehow sets a performance bound on networks. Going from Equation (24) to Equation (25), the input matrix $\mathbf{B}$ and output mode shapes $\mathbf{\Phi}_{out}$ were used. Had the procedure been started from the output matrix $\mathbf{C}$ and input mode shapes $\mathbf{\Phi}_{in}$, this upper bound would have been different, unless $\mathbf{S}$ is set to make these two bounds equal (or almost equal if errors arise due to, e.g., an imperfect experimental identification). To do so, the diagonal matrix $\mathbf{S}$ is selected to minimize the Frobenius norm

$$\mathbf{S} = \arg \min_{\mathbf{S} \text{ diagonal}} \left|\left| \mathbf{S}\mathbf{W}\mathbf{\Omega}_{\mathrm{oc}}^{-1}\mathbf{B}\mathbf{V}_{\mathrm{D}}\mathbf{\Sigma}_{\mathrm{D}}^{-1/2} - \mathbf{S}^{-1}\mathbf{W}\mathbf{\Omega}_{\mathrm{oc}}^{-1}\mathbf{C}^{\mathrm{T}}\mathbf{U}_{\mathrm{D}}\mathbf{\Sigma}_{\mathrm{D}}^{-1/2} \right|\right|^2 . \quad \text{(A.18)}$$

The solution to the least-squares problem given in Equation (A.18) can be found to be given by Equation (33), independently from the normalized mode shapes. This solution also makes the error on Equation (12) minimum in the least-squares sense.

Appendix A.3. Single-mode performance independence on decentralization

To compare cases from fully centralized to fully decentralized in a coherent way, it is assumed that the matrix $\mathbf{D}$ is diagonal, and thus $\mathbf{U}_D = \mathbf{V}_D = \mathbf{I}$ while $\mathbf{\Sigma}_D = \mathbf{D}$. Since a single mode is considered, the weighting coefficients on each group play no role and are set to one for simplicity. Furthermore, the scaling matrix $\mathbf{S}^{(g)}$ reduces to a scalar noted $s^{(g)}$.

From Equation (48) and its unitary constraint, the explicit expression of the optimal dimensionless mode shape on group g is

$$\left(\mathbf{\Psi}^{(g)}\right)^{\star} = \frac{1}{\left|\left| \left(\mathbf{\Sigma}_D^{(g)}\right)^{-1/2} \left(\mathbf{b}_r^{(g)}\right)^T \right|\right|} \left(\mathbf{\Sigma}_D^{(g)}\right)^{-1/2} \left(\mathbf{b}_r^{(g)}\right)^T . \quad \text{(A.19)}$$

Now, Equation (26) shows that the squared MEMCF of group g is

$$\left(\alpha_c^{(g)}\right)^2 = \left(\frac{s^{(g)}}{\omega_{oc,r}} \mathbf{b}_r^{(g)} \left(\mathbf{\Sigma}_D^{(g)}\right)^{-1/2} \left(\mathbf{\Psi}^{(g)}\right)^{\star} \right)^2 = \left(\frac{s^{(g)}}{\omega_{oc,r}} \right)^2 \left|\left| \mathbf{b}_r^{(g)} \left(\mathbf{\Sigma}_D^{(g)}\right)^{-1/2} \right|\right|^2 \quad \text{(A.20)}$$

and, as indicated by Equation (24), the global squared MEMCF is given by the sum of the squared MEMCFs of all groups

$$\alpha_c^2 = \sum_{g=1}^{N_g} \left(\alpha_c^{(g)}\right)^2 = \sum_{g=1}^{N_g} \left(\frac{s^{(g)}}{\omega_{oc,r}} \right)^2 \left|\left| \mathbf{b}_r^{(g)} \left(\mathbf{\Sigma}_D^{(g)}\right)^{-1/2} \right|\right|^2 = \frac{1}{\omega_{oc,r}^2} \mathbf{b}_r \mathbf{\Sigma}_D^{-1} \mathbf{c}_r = \frac{1}{\omega_{oc,r}^2} \mathbf{b}_r \mathbf{D}^{-1} \mathbf{c}_r , \quad \text{(A.21)}$$

which is independent on the way the transducers are distributed among the groups (the last two equalities are deduced using Equations (12) and (35)). Decentralization thus has no effect when a single mode is targeted for vibration reduction.

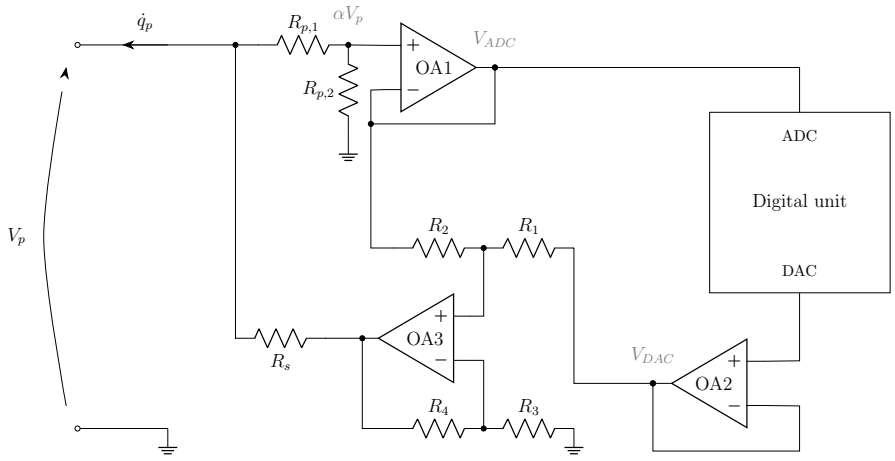

Figure B1: DVA architecture using Howland's current source.

Appendix B. Digital vibration absorbers design

Figure B1 features the architecture of the DVAs used in this work. It is a slight modification of Howland's current source [47, 48], where the resistors labeled $R_{p,1}$ and $R_{p,2}$ have been introduced to attenuate the high piezoelectric voltages in order to avoid saturation of the operational amplifiers (OpAmps). This architecture was favored over that described in [6, 41] because the latter requires floating piezoelectric electrodes, whereas the version used herein allows for grounding one electrode of each transducer, which was imposed by the experimental setup.

Introducing the division ratio

$$\alpha = \frac{R_{p,2}}{R_{p,1} + R_{p,2}}, \tag{B.1}$$

the input and output voltages of OA1 are identical and are fed to the analog-to-digital converter (ADC). They are given by

$$V_{ADC} = \alpha V_p. \tag{B.2}$$

By introducing the amplification gain

$$\beta = 1 + \frac{R_4}{R_3} \tag{B.3}$$

and the attenuation gain

$$\gamma = \frac{R_1}{R_1 + R_2}, \tag{B.4}$$

it is possible to show using the ideal OpAmp assumption [47] that the current injected in the load is a function of the digital-to-analog converter (DAC) voltage as well as the load voltage given by

$$\dot{q}_p = \frac{\beta(1-\gamma)}{R_s} V_{DAC} + \frac{(\alpha\beta\gamma - 1)(R_{p,1} + R_{p,2}) - R_s}{R_s(R_{p,1} + R_{p,2})} V_p = g_c V_{DAC} + \delta_c V_p. \tag{B.5}$$

Table B1: Resistances of the DVAs used in this study.

R_1 (kΩ)	R_2 (kΩ)	R_3 (kΩ)	R_4 (kΩ)	R_s (kΩ)	$R_{p,1}$ (kΩ)	$R_{p,2}$ (kΩ)
10	10	10	115	2.61	49.9	10

Ideally, the current should solely be driven by V_{DAC} and thus δ_c should be zero. While the resistances can be adjusted to closely approach $\delta_c = 0$, it is in general not possible to enforce this condition exactly. It is nevertheless possible to counteract this non-ideal behavior by simply modifying the input-output relation implemented in the digital unit. In order to inject the current $\dot{q}_{Id}$, if instead of merely setting $V_{DAC} = \dot{q}_{Id}/g_c$ (which would be the driving law if $\delta_c = 0$), the DAC voltage is given by

$$V_{DAC} = \frac{1}{g_c}\dot{q}_{Id} - \frac{\delta_c}{g_c\alpha}V_{ADC}, \tag{B.6}$$

then, by Equation (B.5), the current injected into the load is indeed $\dot{q}_{Id}$ (i.e., $\dot{q}_p = \dot{q}_{Id}$). The parameter $\delta_c/(g_c\alpha)$ can be determined from the resistances in the circuit and using Equations (B.1)-(B.5). An alternative that does not require any knowledge about the DVA parameters is to carry out a test when the load is an open circuit ($\dot{q}_p = 0$). Then, by Equations (B.2) and (B.5),

$$V_{ADC} = \alpha V_p = -\frac{\alpha g_c}{\delta_c}V_{DAC}. \tag{B.7}$$

The parameter is thus given by the constant relation between V_{ADC} and V_{DAC} when the load is an open circuit.

The five DVAs used in this study were all built with identical characteristics. The OpAmps are OPA445 from Texas Instruments [49] and the resistances are given in Table B1.

References

[1] Forward R L 1979 *Applied Optics* **18** 690 ISSN 0003-6935 URL `https://www.osapublishing.org/abstract.cfm?URI=ao-18-5-690`

[2] Hagood N and von Flotow A 1991 *Journal of Sound and Vibration* **146** 243–268 ISSN 0022460X URL `https://linkinghub.elsevier.com/retrieve/pii/0022460X91907629`

[3] Gripp J and Rade D 2018 *Mechanical Systems and Signal Processing* **112** 359–383 ISSN 08883270 URL `https://linkinghub.elsevier.com/retrieve/pii/S0888327018302437`

[4] Park C H and Inman D J 2003 *Shock and Vibration* **10** 127–133 ISSN 1070-9622 URL `http://www.hindawi.com/journals/sv/2003/863252/abs/`

[5] Dekemele K, Van Torre P and Loccufier M 2020 *Journal of Vibration and Control* 107754632095261 ISSN 1077-5463 URL `http://journals.sagepub.com/doi/10.1177/1077546320952612`

[6] Fleming A, Behrens S and Moheimani S 2000 *Electronics Letters* **36** 1525 ISSN 00135194 URL `https://digital-library.theiet.org/content/journals/10.1049/el_20001083`

[7] Lossouarn B, Aucejo M, Deü J F and Multon B 2017 *Sensors and Actuators A: Physical* **259** 68–76 ISSN 09244247 URL `https://linkinghub.elsevier.com/retrieve/pii/S0924424716309785`

[8] Berardengo M, Manzoni S, Høgsberg J and Vanali M 2021 *Mechanical Systems and Signal Processing* **151** 107350 ISSN 08883270 URL https://linkinghub.elsevier.com/retrieve/pii/S0888327020307366

[9] Høgsberg J and Krenk S 2017 *Journal of Sound and Vibration* **386** 65–81 ISSN 10958568 URL http://dx.doi.org/10.1016/j.jsv.2016.08.028

[10] Toftekær J F and Høgsberg J 2021 *Journal of Sound and Vibration* **498** 115960 ISSN 0022460X URL https://linkinghub.elsevier.com/retrieve/pii/S0022460X21000328

[11] Moheimani S O R and Fleming A J 2006 *Piezoelectric Transducers for Vibration Control and Damping* Advances in Industrial Control (London: Springer-Verlag) ISBN 1-84628-331-0 URL http://link.springer.com/10.1007/1-84628-332-9

[12] Raze G, Dietrich J and Kerschen G 2022 *Journal of Intelligent Material Systems and Structures* in press URL https://doi.org/10.1177/1045389X221088031

[13] Berardengo M, Manzoni S and Conti A M 2017 *Journal of Sound and Vibration* **405** 287–305 ISSN 10958568 URL http://dx.doi.org/10.1016/j.jsv.2017.06.002

[14] Dal Bo L, He H, Gardonio P, Li Y and Jiang J Z 2022 *Journal of Sound and Vibration* **520** 116554 ISSN 0022460X URL https://linkinghub.elsevier.com/retrieve/pii/S0022460X21005757

[15] Viana F A C and Steffen, Jr V 2006 *Journal of the Brazilian Society of Mechanical Sciences and Engineering* **28** 293–310 ISSN 1678-5878 URL http://www.scielo.br/scielo.php?script=sci_arttext&pid=S1678-58782006000300007&lng=en&nrm=iso&tlng=en

[16] Toftekær J F and Høgsberg J 2020 *Journal of Intelligent Material Systems and Structures* **31** 570–586 ISSN 1045-389X URL http://journals.sagepub.com/doi/10.1177/1045389X19891646

[17] Giorgio I 2008 *Multimode Collocated Vibration Control with Multiple Piezoelectric Transducers* Ph.D. thesis Università degli studi di Roma URL https://tel.archives-ouvertes.fr/tel-00798635

[18] Rosi G 2010 *Control of sound radiation and transmission by means of passive piezoelectric networks : modelling , optimization and experimental implementation* Ph.D. thesis Université Pierre et Marie Curie - Paris VI URL https://tel.archives-ouvertes.fr/tel-00815038

[19] Goodwin G C, Graebe S F and Salgado M E 2001 *Control System Design* (Upper Saddle River, NJ: Prentice Hall) ISBN 978-0139586538 URL https://www.pearson.ch/HigherEducation/Pearson/EAN/9780139586538/Control-System-Design

[20] Engels W P, Baumann O N, Elliott S J and Fraanje R 2006 *The Journal of the Acoustical Society of America* **119** 1487–1495 ISSN 0001-4966 URL http://asa.scitation.org/doi/10.1121/1.2163270

[21] Alessandroni S, Dell'Isola F and Porfiri M 2002 *International Journal of Solids and Structures* **39** 5295–5324 ISSN 00207683 URL https://linkinghub.elsevier.com/retrieve/pii/S002076830200402X

[22] Lossouarn B, Deü J F and Aucejo M 2015 *Smart Materials and Structures* **24** 115037 ISSN 0964-1726 URL https://iopscience.iop.org/article/10.1088/0964-1726/24/11/115037

[23] Lossouarn B, Deü J F, Aucejo M and Cunefare K A 2016 *Smart Materials and Structures* **25** 1–15 ISSN 1361665X URL http://dx.doi.org/10.1088/0964-1726/25/11/115042

[24] Darleux R, Lossouarn B, Giorgio I, Dell'Isola F and Deü J F 2021 *Mathematics and Mechanics of Solids* 108128652110276 ISSN 1081-2865 URL http://journals.sagepub.com/doi/10.1177/10812865211027622

[25] Lossouarn B, Kerschen G and Deü J F 2021 *Journal of Sound and Vibration* **511** 116323 ISSN 0022460X URL https://linkinghub.elsevier.com/retrieve/pii/S0022460X21003825

[26] Moheimani S, Fleming A and Behrens S 2004 *IEEE/ASME Transactions on Mechatronics* **9** 87–99 ISSN 1083-4435 URL http://ieeexplore.ieee.org/document/1275482/

[27] Giorgio I, Culla A and Del Vescovo D 2009 *Archive of Applied Mechanics* **79** 859–879 ISSN 0939-1533 URL http://link.springer.com/10.1007/s00419-008-0258-x

[28] Raze G, Dietrich J, Lossouarn B and Kerschen G 2022 *Mechanical Systems and Signal Processing*

176 109120 ISSN 0888-3270 URL https://www.sciencedirect.com/science/article/pii/S0888327022002850

[29] Trindade M A, Lossouarn B and Deü J F 2021 *Journal of Intelligent Material Systems and Structures* **32** 971–985 ISSN 1045-389X URL http://journals.sagepub.com/doi/10.1177/1045389X20942847

[30] Thomas O, Deü J F and Ducarne J 2009 *International Journal for Numerical Methods in Engineering* **80** 235–268 ISSN 00295981 URL http://doi.wiley.com/10.1002/nme.2632

[31] Larbi W and Deü J F 2019 *Applied Acoustics* **147** 111–120 ISSN 0003682X URL https://linkinghub.elsevier.com/retrieve/pii/S0003682X17307028

[32] McKelvey T, Akcay H and Ljung L 1996 *IEEE Transactions on Automatic Control* **41** 960–979 ISSN 00189286 URL http://ieeexplore.ieee.org/document/508900/

[33] Juang J N and Pappa R S 1985 *Journal of Guidance, Control, and Dynamics* **8** 620–627 ISSN 0731-5090 URL https://arc.aiaa.org/doi/10.2514/3.20031

[34] Peeters B, Van der Auweraer H, Guillaume P and Leuridan J 2004 *Shock and Vibration* **11** 395–409 ISSN 1070-9622 URL http://www.hindawi.com/journals/sv/2004/523692/abs/

[35] Soltani P, Kerschen G, Tondreau G and Deraemaeker A 2014 *Smart Materials and Structures* **23** 125014 ISSN 0964-1726 URL http://stacks.iop.org/0964-1726/23/i=12/a=125014?key=crossref.798743ce34b627bed945b046d8a6b51a

[36] Thomas O, Ducarne J and Deü J F 2012 *Smart Materials and Structures* **21** 015008 ISSN 0964-1726 URL https://iopscience.iop.org/article/10.1088/0964-1726/21/1/015008

[37] Raze G, Dietrich J and Kerschen G 2021 *Journal of Sound and Vibration* **515** 116490 ISSN 0022460X URL https://linkinghub.elsevier.com/retrieve/pii/S0022460X21005253

[38] Ikegame T, Takagi K and Inoue T 2019 *Journal of Vibration and Acoustics* **141** 031015 ISSN 1048-9002 URL https://asmedigitalcollection.asme.org/vibrationacoustics/article/doi/10.1115/1.4042819/727600/Exact-Solutions-to-H-and-H2-Optimizations-of

[39] Raze G, Dietrich J and Kerschen G 2022 *Journal of Intelligent Material Systems and Structures* 1045389X211072269 URL https://doi.org/10.1177/1045389X211072269

[40] Swamy K 1973 *IEEE Transactions on Automatic Control* **18** 306–306 ISSN 0018-9286 URL http://ieeexplore.ieee.org/document/1100319/

[41] Raze G 2021 *Piezoelectric Digital Vibration Absorbers for Multimodal Vibration Mitigation of Complex Mechanical Structures* Ph.D. thesis Université de Liège URL http://hdl.handle.net/2268/256608

[42] Ewins D J 2009 *Modal testing: theory, practice and application* (John Wiley & Sons) URL https://www.wiley.com/en-us/Modal+Testing%3A+Theory%2C+Practice+and+Application%2C+2nd+Edition-p-9780863802188

[43] Berardengo M, Manzoni S and Vanali M 2016 *Shock and Vibration* **2016** 1–18 ISSN 1070-9622 URL https://www.hindawi.com/journals/sv/2016/9739217/

[44] Maurini C, Pouget J and Dell'Isola F 2006 *Computers & Structures* **84** 1438–1458 ISSN 00457949 URL https://linkinghub.elsevier.com/retrieve/pii/S0045794906000885

[45] Gannett J and Chua L 1978 Frequency Domain Passivity Conditions for Linear Time-Invariant Lumped Networks Tech. Rep. Technical Report No. UCB/ERL M78/21 EECS Department, University of California, Berkeley Berkeley URL https://www2.eecs.berkeley.edu/Pubs/TechRpts/1978/28925.html

[46] Ten Berge J M F 1983 *Psychometrika* **48** 519–523 ISSN 0033-3123 URL http://link.springer.com/10.1007/BF02293876

[47] Horowitz P and Hill W 2015 *The Art of Electronics* 3rd ed (Cambridge University Press) ISBN 978-0-521-37095-0

[48] Necasek J, Vaclavik J and Marton P 2017 Comparison of analog front-ends for digital synthetic impedance device *2017 IEEE International Workshop of Electronics, Control, Measurement, Signals and their Application to Mechatronics (ECMSM)* (IEEE) pp 1–4 ISBN 978-1-5090-5582-1 URL http://ieeexplore.ieee.org/document/7945916/

[49] TI 2008 High Voltage FET-Input Operational Amplifier URL `https://www.ti.com/product/OPA445`